ENHANCING ELECTRIC VEHICLE SAFETY: AI-DRIVEN MULTIPHYSICS APPROACH FOR PREDICTING THERMAL FAILURES IN LI-ION BATTERIES

by

Basab Ranjan Das Goswami

A Dissertation Submitted to the Faculty of the

DEPARTMENT OF AEROSPACE AND MECHANICAL ENGINEERING

In Partial Fulfillment of the Requirements

For the degree of

DOCTOR OF PHILOSOPHY

In the Graduate College

THE UNIVERSITY OF ARIZONA

2024

THE UNIVERSITY OF ARIZONA
GRADUATE COLLEGE

As members of the Dissertation Committee, we certify that we have read the dissertation prepared by Basab Ranjan Das Goswami, titled Electric Vehicle Safety: AI-Driven Multiphysics Approach for Predicting Thermal Failures in Li-Ion Batteries and recommend that it be accepted as fulfilling the dissertation requirement for the Degree of Doctor of Philosophy.

Vitaliy Yurkiv _____ Date: 07/23/2024
Vitaliy Yurkiv

Farzad Mashayek _____ Date: 07/23/2024
Farzad Mashayek

_____ Date: 07/23/2024
Kyle Hanquist

_____ Date: 07/23/2024
Majid Beidaghi

Final approval and acceptance of this dissertation is contingent upon the candidate's submission of the final copies of the dissertation to the Graduate College.

I hereby certify that I have read this dissertation prepared under my direction and recommend that it be accepted as fulfilling the dissertation requirement.

Vitaliy Yurkiv _____ Date: 07/23/2024
Vitaliy Yurkiv
Dissertation Committee Chair
Aerospace and Mechanical Engineering

ACKNOWLEDGMENTS

This dissertation stands as a testament not only to my academic endeavors but also to the incredible support that has buoyed me through this journey. At the forefront are my parents, whose boundless love and unwavering belief in my potential have been the bedrock of my accomplishments. Their sacrifices and guidance have not only shaped me as an individual but have also been the cornerstone of every step I have taken in this academic journey. For this, I am eternally grateful.

I extend my heartfelt gratitude to my supervisor, Prof. Vitaliy R. Yurkiv. His mentorship has been nothing short of transformative. Prof. Yurkiv has been a source of knowledge and enlightenment, guiding me through the complexities of energy storage technologies and artificial intelligence. His expertise and encouragement have been instrumental in shaping my research direction and professional growth. His commitment to excellence and innovation has opened new horizons for me, for which I am profoundly thankful.

To the esteemed members of my committee, Dr. Farzad Mashayek, Dr. Majid Beidaghi, and Dr. Kyle Hanquist, your insightful feedback and constructive criticism have been invaluable. Your dedication and support have significantly enhanced the quality of my work, helping me to refine my thesis and navigate the challenges of research with confidence.

Lastly, to my friends who have been my source of joy and strength, your camaraderie and shared experiences have made this journey memorable. Your support has transcended geographical boundaries and cultural differences, proving that true friendship knows no bounds. In closing, my journey thus far has been enriched and made possible by each one of you. My deepest gratitude to all for your relentless support, encouragement, and belief in my abilities.

TABLE OF CONTENTS

LIST OF TABLES

LIST OF FIGURES

DEDICATION

"*Your work is going to fill a large part of your life, and the only way to be truly satisfied is to do what you believe is great work. And the only way to do great work is to love what you do. If you haven't found it yet, keep looking. Don't settle. As with all matters of the heart, you'll know when you find it.*"

-Steve Jobs

To my Maa and Baba. Thank you for all the hope you gave and the sacrifices you made.

ABSTRACT

The focus of this dissertation is to address the critical issue of safety in lithium-ion batteries (LIBs), particularly focusing on thermal runaway (TR), a significant threat to their reliability and widespread adoption. With the surge in demand for energy storage driven by electric vehicles (EVs) and renewable energy uptake, ensuring LIB safety is paramount. The research innovatively combines advanced machine learning (ML) techniques with multiphysics modeling to predict and prevent TR incidents. Initially, I applied convolutional neural networks (CNNs) and the "you look only once" (YOLO) object detection model to forecast TR in single LIBs. This phase leveraged simulated thermal images generated by a comprehensive multiphysics model that incorporates thermal, electrochemical, and degradation processes, particularly focusing on solid electrolyte interface (SEI) dynamics. The models demonstrated high accuracy in predicting TR stages and pinpointing heat sources within a battery. Expanding this approach, the I, then developed a novel ML framework to address TR in LIB modules, which is crucial for EV safety. This framework integrates graph neural networks (GNN) for spatial analysis and Long Short-Term Memory (LSTM) networks for temporal predictions, which are trained on sensor-derived temperature data. The advanced model effectively identified spatio-temporal temperature variations and potential hotspots within battery modules, offering real-time insights to avert TR. This research significantly advances the safety and reliability of LIBs by integrating cutting-edge ML with detailed multiphysics modeling. It marks a substantial step towards safer, more sustainable energy storage solutions, contributing to the broader goal of a low-carbon future by enhancing LIB integration in diverse applications, from portable electronics to EVs and renewable energy systems.

CHAPTER 1. INTRODUCTION

1.1 Overview of energy storage technologies

Energy storage technologies play a crucial role in bridging the temporal gap between energy production and consumption, particularly in an era where the shift toward renewable energy sources is paramount. These technologies not only facilitate the increased incorporation of intermittent renewable energies, such as solar and wind, into the grid but also enhance grid stability and reliability. The landscape of energy storage is vast and diverse, encompassing mechanical, electrochemical, thermal, and chemical storage solutions, each with its unique attributes and suited for different applications within the energy sector. These technologies can broadly be classified into categories such as mechanical, electrochemical (including batteries), thermal, and chemical storage, each serving distinct purposes and applications in the energy landscape. Mechanical Storage Methods, such as Pumped Hydroelectric Storage (PHS), capitalize on gravitational potential energy. By pumping water to elevated reservoirs during times of excess energy and then releasing it to generate electricity on demand, PHS offers a mature and scalable solution for energy storage, critical for grid balancing and management [1]. Chemical Storage involves the conversion of electricity into chemical energy, which can be stored for long periods and then reconverted into electrical energy when needed. While offering high energy density and storage capacity, chemical storage methods, such as hydrogen fuel cells, face challenges in efficiency, cost, and the need for significant infrastructure development [2,3]. Thermal Energy Storage (TES) technologies, like molten-salt storage, store heat energy that can be later converted into electricity or used directly for heating and cooling applications. TES systems are integral to the integration of renewable energy, enabling the decoupling of energy supply from immediate demand [3]. As the share of

variable renewable energy sources grows, the need for effective and efficient energy storage solutions becomes increasingly crucial. Amidst the diverse spectrum of energy storage technologies, Electrochemical Storage, and more specifically, Lithium-Ion Batteries (LIBs), have emerged as a linchpin in the current and future landscape of energy storage. LIBs stand as a pinnacle of electrochemical storage technology, marking a significant milestone in the journey toward efficient, reliable, and sustainable energy solutions. When we examine mechanical, thermal, and chemical energy storage technologies alongside lithium-ion batteries (LIBs), it becomes evident why LIBs are often preferred for a broad spectrum of applications. While each type of energy storage has its strengths and plays a crucial role in diversifying the energy storage mix, several factors distinguish LIBs as particularly versatile and efficient. For instance, while PHS is invaluable for grid stability and can store energy for extended periods, its deployment is geographically limited and often involves substantial environmental and financial costs. These constraints make PHS less adaptable, especially in areas lacking the necessary topographical features or where environmental concerns are paramount. The efficiency of TES systems can be lower than that of electrochemical storage solutions like LIBs. The conversion of stored thermal energy back into electricity introduces energy losses, and the materials and infrastructure required for TES can be cost-prohibitive, limiting its widespread adoption. In contrast, lithium-ion batteries offer several advantages that address these limitations. Their high energy density and efficiency mean that LIBs can store more energy in a smaller, lighter package and with less energy lost during charging and discharging cycles. This makes LIBs ideal for a wide range of applications, from portable electronics to electric vehicles and grid storage. Furthermore, LIBs are not constrained by geographical limitations, allowing for deployment in diverse settings, including urban areas and remote locations [4]. The flexibility and scalability of LIBs, coupled with rapidly declining costs

due to technological advancements, have made them increasingly economically viable. The essence of LIB technology lies in its ingenious use of lithium ions, which move between the anode and cathode through an electrolyte during charging and discharging cycles. This movement, facilitated by the lightweight and highly reactive nature of lithium, allows for the efficient storage and release of energy, setting LIBs apart in terms of efficiency and energy density. The evolution of LIBs has seen a transition towards safer and more durable materials, with variations such as lithium manganese oxide, lithium iron phosphate, and lithium nickel manganese cobalt oxides, enhancing the battery's safety, lifecycle, and energy storage capacity. This evolution underscores a relentless pursuit of excellence in battery technology, aiming to meet the ever-growing demands of modern energy needs. What distinguishes lithium-ion batteries from other storage technologies is a constellation of advantages that cater to a wide range of applications. They possess an unparalleled energy density, which allows them to store more energy per unit of weight than most alternatives. This characteristic, coupled with high charge and discharge efficiencies that hover around 90-95%, ensures minimal energy loss and makes LIBs exceptionally suitable for applications where weight, space, and efficiency are crucial. Furthermore, their versatility allows for deployment in virtually any setting without the geographical or environmental constraints typical of mechanical or thermal storage systems. The scalability of LIBs, from powering the smallest of portable electronics to energizing large-scale grid storage systems, illustrates their adaptability across a spectrum of energy requirements. Additionally, advances in technology have steadily improved their lifespan and reduced the rate of capacity loss, enhancing their economic and environmental appeal. The applications of lithium-ion batteries are as varied as they are impactful. In the realm of portable electronics, LIBs have become the de facto standard, powering devices that are integral to daily life, such as smartphones and laptops. The automotive industry

has been revolutionized by the adoption of LIBs in electric vehicles, significantly reducing carbon emissions and paving the way for a sustainable transportation future [5]. Moreover, the integration of renewable energy sources into the power grid has been greatly facilitated by LIBs, which store excess energy generated from wind and solar sources, thereby stabilizing the grid and ensuring a consistent energy supply. Their utility extends into industrial applications, including power tools and large-scale energy storage systems that provide critical services such as uninterrupted power supplies and peak shaving. Looking ahead, the trajectory of lithium-ion battery technology is marked by promising innovations and an unwavering commitment to improvement. The advent of solid-state batteries, which substitute liquid electrolytes with a solid, is poised to further elevate the safety and energy density of LIBs. Concurrently, the sustainability of battery technology is being addressed through advances in recycling processes, aimed at mitigating environmental impacts and reclaiming valuable materials. The global market for LIBs is on an exponential growth curve, fueled by the surging demand for electric vehicles, renewable energy storage, and the ubiquity of portable electronic devices. This growth is underpinned by significant investments in battery manufacturing and recycling infrastructure, which are making LIBs increasingly cost-effective and accessible [6].

In essence, lithium-ion batteries encapsulate the dynamic interplay between innovation, efficiency, and sustainability in the energy storage domain. Their continuous development and integration into various facets of modern life not only highlights their critical role in the energy transition but also underscores their potential to shape a more sustainable and energy-efficient future.

1.2 Multiphysics modeling of batteries

The widespread utilization of batteries has spurred investigations into creating designs that are both safe and efficient. However, implementing these studies practically poses significant challenges. For example, investigating the effect of a design parameter on battery performance entails constructing and observing multiple battery setups. For instance, examining how a design factor influences battery performance involves creating and observing numerous battery configurations [7,8]. This challenge becomes more pronounced in battery optimization research, where the design necessitates iterative enhancements. In alternative studies, dormant areas within the battery are pinpointed to improve the utilization of battery materials. This necessitates identifying electrochemical and thermal characteristics at various locations within the battery. Additionally, these measurements should not disrupt battery processes, which is challenging due to the thinness of certain systems, such as layers in Li-ion batteries, which can be less than a millimeter thick. Furthermore, there is increasing interest in thermal management and safety systems, the design of which can be expensive to accomplish solely through experiments [9,10].

The drawbacks of experimental methods are overcome through multiphysics modeling. Such modeling integrates fundamental principles and equations from diverse fields to forecast the performance of a battery system. These equations are concurrently solved to capture the interconnectedness of physical and chemical attributes. This approach proves cost-effective since battery behavior is simulated computationally. Moreover, the progression of physical and chemical properties within the battery system over time emerges organically from solving the governing equations. Typically, these models depict the battery at a macroscopic scale, employing variables like concentration, potential, current density, and heat generation. One of the widely embraced multiphysics models was formulated by Doyle, Newman, and Fuller for lithium-ion batteries. This

model drew upon Newman's porous electrode theory and concentrated electrolyte theory as its foundation [11]. Tiedemann and Newman introduced the lead-acid multiphysics model back in 1979, followed by Gu et al.'s enhancement in 1987, which incorporated charge and rest behavior [12]. Nevertheless, these groundbreaking models are limited to forecasting the electrochemical performance of a battery solely under ideal circumstances. To address this, multiphysics models have been devised to accommodate adverse occurrences such as thermal runaway in lithium-ion batteries [13].

1.3 Machine learning in battery research

Ensuring the well-being and safety of batteries is vital for their various uses. Nevertheless, battery deterioration is an unavoidable occurrence. Hence, there's a pressing necessity to implement a battery management system (BMS) to precisely assess battery conditions and forecast their longevity. Various models, including electrochemical and equivalent circuit models, have been suggested to achieve real-time estimation of battery states. Nonetheless, the significant drawbacks of multiphysics simulations are their high computational demands and the presence of quantitative inaccuracies in the simulations. In recent years, ML models have emerged for precise forecasting of battery conditions. Unlike conventional models, ML models excel at anticipating battery states prior to capacity decline, thus substantially cutting down monitoring expenses. ML has been extensively used in different areas of battery research at different length scales, from fundamental studies of structural properties to end-use applications like EVs. In the studies of structure properties, ML methods have shown to be promising techniques for the investigation of the structure-properties relationships and the understanding of the behavior of the materials employed in LIBs [14–16]. Another area of research related to LIBs and ML is the battery state-of-charge

(SOC) estimation for EVs [17,18]. This has gained significant recognition in recent times due to the extensive development of EVs. Moreover, there have been significant works on the application of ML to estimate the SOH (State of Health), SOC, and RUL (Remaining Useful Life) using methods such as XGBoost, random forest, and k-nearest neighbor algorithm (KNN) [19,20]. Similarly, ML models are also applied in LIBs prognostics [21]. Additionally, ML methods, namely support vector machine (SVM), relevance vector machine (RVM) [22], and Gaussian process regression (GPR) [23,24] have been widely used in this area of research. Deep learning (DL) methods like artificial neural networks (ANNs) [25] have been utilized in the area of battery design and health monitoring. Recently, Transformer models have become increasingly popular in various aspects of time-series analysis. They tackle the complexities involved using self-attention mechanisms and positional encodings. These strategies allow them to simultaneously focus on immediate data samples and capture the details of their sequence. The Transformer's architecture is specifically designed to identify relationships between different input segments by incorporating positional information and employing the dot product operation [26,27]. In the context of batteries, Shi et al. [28] have developed a specialized Transformer-based network, BERTtery, to accurately estimate the SOC for electric vehicles using time-resolved battery data. This highlights its potential for practical application in predicting the behavior of complex battery systems in EVs. Shen et al. [29]have introduced a novel approach for state-of-charge (SOC) estimation in lithium-ion batteries using a Transformer neural network combined with an immersion and invariance (I&I) adaptive observer. The Transformer model utilizes sequences of current, voltage, and temperature data to predict SOC, while the I&I adaptive observer minimizes oscillations in the Transformer's predictions. Experimental validation showed that this method outperforms conventional SOC estimation techniques, ensuring higher accuracy and stability in battery parameter estimation.

Recently, there have been reports of DL/ML models [30,31], which include the prediction of simulated/ experimental results at reduced computational costs for inspecting and forecasting thermal failures in batteries. The subsequent section reviews past publications on the application of ML in predicting battery thermal failures.

1.3.1 Machine learning for battery thermal failures

Batteries, as complex materials systems, pose unique challenges for the application of ML especially for thermal management or safety from thermal failures. Although a shift to data-driven, ML-based battery safety research has started, new initiatives in academia and industry are still needed to exploit its potential fully. In this context, Lee et al. [32] introduced a method to convert partial charging data into a statistical entity called the likelihood vector. These vectors were computed using possibility distribution functions derived from experimental voltage and current data, simulating various degradation and abuse conditions for LIBs. Compared to the brute-force training method that uses partial charging curves to train MLP classifier models, utilizing likelihood vectors for training significantly improved test set classification accuracy by 26–85%, depending on the neural network size. Additionally, monitoring the failure index from the cumulative detection list experimentally showed that the TR and resultant fatal explosion event of a lithium pouch cell during an operando dent test could be predicted before occurrence. Similarly, Jiang et al. [33] proposed a novel data-driven method for LIB pack fault diagnosis and TR warning based on state representation methodology. Their results demonstrated that the method could accurately identify faulty cells, determine the type of voltage fault, and provide early fault detection and TR warnings. Furthermore, Ding et al. [34] presented a data-driven approach to accurately forecast battery TR state at the cell level using a meta TR forecasting neural network (Meta-TRFNN). Testing with both simulated and real-world samples showcased the forecasting

capability of Meta-TRFNN, the advantages of using high-dimensional thermal images, and the efficacy of the meta-learning framework. Additionally, Yang et al. [35] applied an extreme learning machine (ELM)-based thermal (ELMT) model to predict battery temperature behavior under an external short circuit, replacing the conventional ELM activation function with a lumped-state thermal model. When compared to a multi-lumped-state thermal (MLT) model parameterized by a genetic algorithm using experimental data from various battery cells, the ELMT model demonstrated higher computational efficiency and better fitting and prediction accuracy. Moreover, Ojo et al. [36] developed an LSTM-based NN model combined with the newly introduced stretch-forward technique and residual monitor to detect faults. The experimental results indicated that this approach could accurately estimate the cell surface temperature, showing good predictive accuracy and fault detection performance. Da Li et al. [37] proposed a thermal runaway prognosis model based on abnormal heat generation, combining LSTM and CNN. The verification results indicated that the proposed scheme could accurately predict battery temperature 48 time-steps ahead with a mean-relative error of 0.28% across all seasons, demonstrating its robustness and adaptability. Additionally, the model could provide a 27-minute-ahead TR prognosis, with 19 minutes from the abnormal heat generation diagnosis method and 8 minutes from the CNN-LSTM approach. It is evident that a growing number of ML methods are being developed and applied to various aspects of battery safety, including internal and external short circuits, temperature prediction, and failure diagnosis.

1.4 Motivation

LIBs have emerged as a dominant energy storage technology, powering a wide range of applications, from portable electronics to electric vehicles and renewable energy systems [38]. Their high energy density, long cycle life, and light weight make them highly desirable for many

modern applications. However, despite their advantages, Li-ion batteries are also associated with safety concerns, especially the risk of TR events that can lead to catastrophic failure and safety hazards. TR refers to the uncontrolled increase in temperature within a battery cell or a battery module, resulting from a self-sustaining chain reaction of exothermic chemical reactions [39,40]. It can occur due to various factors, such as overcharging, over-discharging, high-temperature exposure, manufacturing defects, and internal short circuits [41]. The rapid temperature rise during TR can lead to thermal and mechanical stresses, gas generation, electrolyte decomposition, and ultimately, battery failure, including venting, fire, or explosion. Accurate prediction of TR is crucial for ensuring the safety and reliability of Li-ion batteries in various applications. One approach to predicting TR is through mathematical modeling [39,42], which involves the development of mathematical equations based on fundamental physical principles to describe the complex phenomena occurring within a battery during TR. Such models can provide insights into the thermal behavior of Li-ion batteries, aid in the design and optimization of battery systems, and help in the development of effective thermal management strategies. In recent years, there has been increasing interest in the use of ML methodologies in battery research [17–19,43–45], including the prediction of TR events [46,47]. ML techniques, such as artificial neural networks, support vector machines [22], and decision trees [23], can analyze large amounts of data and identify complex patterns and correlations that may not be easily discernible through traditional mathematical modeling. This has led to the emergence of combined multiphysics simulation and ML methodologies as a promising approach for predicting TR in battery modules, as it allows for the integration of physics-based models with data-driven algorithms for improved prediction accuracy.

In this research, ML and DL techniques have been combined with multiphysics simulations to investigate the thermal aspects of LIBs, with the aim of predicting and prevention of thermal failures. The motivation of the present work is deeply rooted in the rapidly growing demand for EVs and the crucial role of LIBs in this sector. Safety concerns surrounding these batteries, particularly regarding TR incidents, highlight the need for enhanced safety measures. The advancement in artificial intelligence and machine learning technologies offers an unprecedented opportunity to tackle these safety challenges. This research not only aims to fill a significant gap in integrating AI with battery technology but also aligns with global initiatives for sustainable energy and environmental conservation. By improving the safety and reliability of EV batteries, the thesis contributes substantially to the sustainable evolution of transportation technology.

1.5 Research objectives

The objective of my research is to predict and prevent thermal failures in LIBs by deploying AI algorithms based on ML and DL models integrated with multiphysics simulations of the battery and its components.

1. Develop an integrated multiphysics and machine learning framework: To create a comprehensive system that combines multiphysics modeling with advanced machine learning techniques for predicting thermal failures in LIBs.
2. Predict and prevent TR in LIBs: Utilize the developed framework to accurately predict the occurrence of thermal runaway events, with the ultimate goal of preventing such failures to enhance battery safety.

3. Optimize battery safety for EVs: Apply the research findings to improve the safety and reliability of lithium-ion batteries in electric vehicles, addressing one of the most pressing concerns in the EV industry.
4. Advance the understanding of battery degradation mechanisms: Investigate the key factors leading to battery degradation, particularly focusing on the SEI decomposition and how this influences the thermal stability of batteries.
5. Innovate machine learning applications in battery research: Explore and refine the use of various machine learning methodologies, such as CNNs and deep learning frameworks, for the analysis and prediction of battery performance and safety.
6. Contribute to sustainable energy solutions: By enhancing the safety and reliability of lithium-ion batteries, the research aims to support the broader adoption of electric vehicles, contributing to the global effort towards sustainable energy and reduced carbon emissions.

1.6 Thesis organization

This thesis is structured in 4 chapters. In **Chapter 1**, a detailed introduction and background of the work are presented, along with a relevant literature review on the mathematical modeling of LIBs and the application of machine learning in battery research. **Chapter 2** introduces a combined approach involving multiphysics models, thermal imaging, and machine learning algorithms for predicting thermal runaway in lithium-ion batteries. Safety in battery operation is paramount, with a focus on accurately identifying and preventing catastrophic events in commonly used cylindrical LIBs. Building upon the results shown in chapter 2, **Chapter 3** extends the single cell model to a battery module level for EVs. This chapter discusses a novel approach that combines multiphysics simulation with machine learning for TR prediction in

battery modules. It focuses on liquid-cooled Panasonic 2170 cells, models a unit of four cells due to computational constraints, considers SEI decomposition as a degradation mechanism, and artificially introduces hotspots for testing. Two load cycles are applied to simulate real EV behavior, and thermocouples measure the temperature on the battery surface. Traditional methods prove inadequate, so a GNN-LSTM network is developed to predict future temperature trends, aiding in TR prediction. This hybrid approach integrates physics-based modeling and data-driven ML for effective TR prediction in battery modules. **Chapter 4** presents the final summary of the entire dissertation and possible future directions for the work.

CHAPTER 2. PREDICTING THERMAL RUNAWAY IN A SINGLE BATTERY

In this chapter, the multiphysics models, the ML and DL algorithms, as well as the fundamental assumptions and the implementation procedures adopted in this work, are described. This chapter delves into the critical challenge of thermal runaway in lithium-ion batteries, a major safety concern. It presents a novel approach combining multiphysics modeling (incorporating thermal and electrochemical dynamics) with deep learning algorithms. The primary objective presented in this chapter is to develop a combined multiphysics and ML-based approach to predict and prevent the TR in LIBs using thermal images of the battery during operation. The supporting objective is to provide the safety aspects of LIBs operation derived from the multiphysics-informed ML techniques. For the multiphysics model, the Panasonic 18650 cylindrical cell has been considered. This cell utilizes Graphite as the negative electrode and Nickel Manganese Cobalt (NMC) as the positive electrode. Since the SEI decomposition sets a pathway for thermal runaway, the SEI decomposition has been considered as the major degradation mechanism in the multiphysics model. Additionally, multiple high-temperature hotspots have been considered at different locations within the battery. From the multiphysics model, thermal images have been generated as sequences of video frames during the battery operation. Next, the extracted images are used for the application of various ML methodologies. In the ML study, a classification technique has been employed using various convolutional neural networks (CNNs) to predict the TR. For this purpose, three labels have been considered, namely, safe, critical, and the TR. The selection of these labels is solely dependent on the maximum surface temperature of the battery, which is explained in detail in the methodology section. Finally, an advanced application of ML has been utilized, known as object detection [48], a technique that has not previously been used in the area of the TR, for the detection of high-temperature hotspots in the battery, which could lead

to the TR. This integrated framework is designed to accurately predict the onset and stages of thermal runaway, a phenomenon where excessive heat generation can lead to catastrophic battery failures. The chapter's focus is on enhancing safety by providing a more reliable method for predicting these events in cylindrical Li-ion batteries, which are commonly used in various electronic devices and electric vehicles.

2.1 Multiphysics based deep learning framework for battery degradation and hotspot detection

In this section, the general workflow of the framework that has been carried out is described. First, a computational approach has been developed to investigate battery degradation using an electrochemical-thermal model of LIBs. This is followed by the acquisition of thermal images from the simulations after undergoing further data preprocessing. Then, these images are fed into the DL network for the classification task of predicting three labels related to the TR event. Finally, the detection of high-temperature hotspots in the battery using an object detection technique is performed. Figure 1 shows the class of systems modeled in this work (left-hand side) together with the ML workflow (right-hand side).

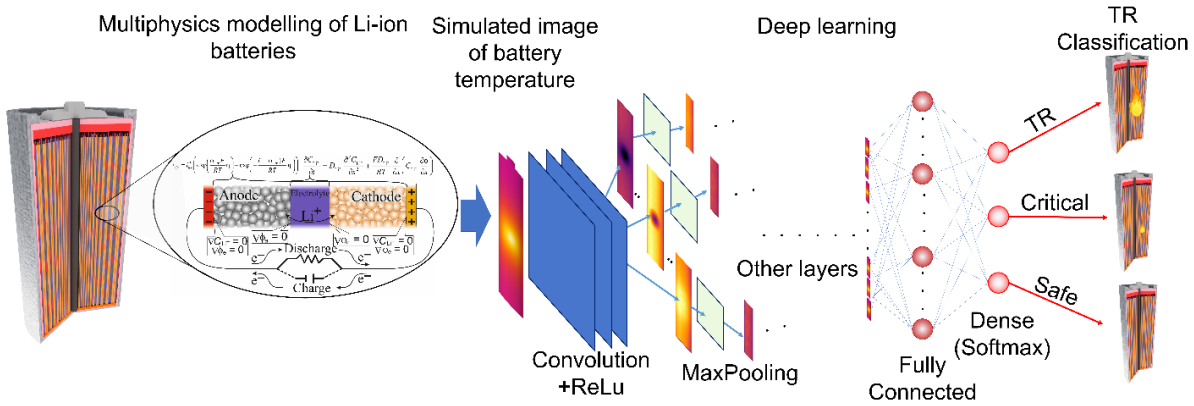

Fig. 1. Schematic illustration of physics-informed ML study to predict and identify the TR in cylindrical type LIBs. The multiphysics modeling (left-hand side image) of the cylindrical cell is used to create a data set for ML (middle image), allowing to identify and forecast of the TR in LIBs. Note: the images on the left are not to scale, merely for illustration purposes.

2.1.1 Multiphysics modeling methodology

In this section, the methodology involving the multiphysics model is described. First, the general electrochemical model is discussed, followed by a description of the thermal model. Additionally, the initial and boundary conditions for the model, followed by a general introduction involving the model implementation, have been discussed. The multiphysics model utilizes the finite element method (FEM) to simulate the electrochemical-thermal behavior of a cylindrical battery type at various conditions. The P2D model [49–51] is used for modeling electrochemistry, and a 3D model has been used to simulate the battery temperature. The two models are then coupled by the generated heat source and the temperature. Highlighting the pivotal role of the P2D model, its reputation is built on a foundation of exceptional accuracy when compared to experimental data. Doyle and Newman's influential work has unequivocally demonstrated the effectiveness of the P2D model through direct comparisons with experimental results [52]. Notably, the outcomes exhibit commendable alignment with experimental data, particularly in scenarios involving non-uniform SEI growth. This robust validation underscores the reliability and effectiveness of the P2D model in capturing real-world phenomena, further affirming its credibility in our work. This model consists of three regions, i.e., the "negative electrode-separator-positive electrode." Below are some of the main features of the P2D model:

1. The P2D model represents a 1D continuum description of the battery, assumes porous electrodes as spheres, and uses the 1D cross-section of the cell to simulate the flow of ions during the charge and discharge of the battery [49].

2. The Butler-Volmer equation [50] (cf. Eq. 11) is used to model the electrochemical charge transfer reaction at the interface of the electrodes and the electrolytes.

3. Equations for binary electrolytes are utilized to model material balance and ionic charge balances in the electrolyte.

4. Transport properties in the electrode are modeled using a homogenization approach (the Bruggeman relation).

The general schematic of the model is shown in Fig. 2.

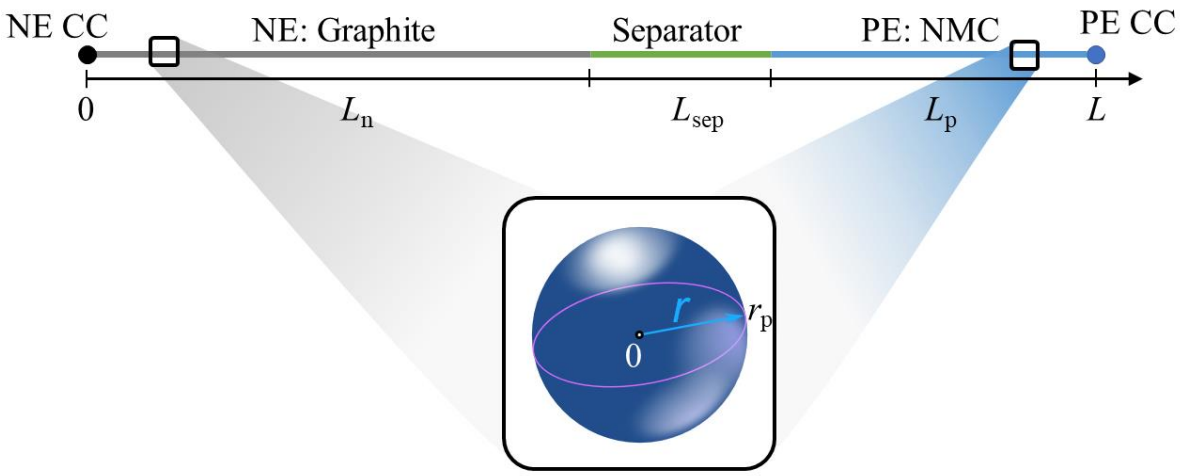

Fig. 2. Schematic of the computational domain for the P2D model of a Li-ion battery.

The governing equations are solved for four dependent variables

• ϕ_s, the electrode potential (solid phase potential),

• ϕ_l, the electrolyte potential (electrolyte phase potential),

• c_s, the concentration of lithium ions in the solid phase,

• c_l, the concentration of lithium ions in the electrolyte phase.

Mass conservation in the solid phase

The transport equation for the solid phase is given by Fick's second law of diffusion as

$$\frac{\partial c_s}{\partial t} = -\nabla \cdot (-D_s \nabla c_s), \tag{1}$$

Boundary conditions are assigned as

$$-D_s \frac{\partial c_s}{\partial r}|_{r=0} = 0, \quad -D_s \frac{\partial c_s}{\partial r}|_{r=r_p} = -R_\theta, \tag{2}$$

where R_θ denotes the molar flux of the cation at the particle surface, caused by the electrochemical insertion reactions.

Charge conservation in solid phase

The charge conservation in the solid phase in given by combining the generalized Ohm's law and the Faraday law as

$$\nabla \cdot \left(-\sigma_{s,\text{eff}} \nabla \phi_s\right) = -i_{v,\text{total}} + Q_s. \tag{3}$$

Note: Q_s is an additional source term which is considered 0 in our case.

Boundary conditions are given by

$$-\sigma_{s,\text{eff}} \nabla \phi_s|_{x=0,L} = \frac{I_{\text{app}}}{A}, \qquad \nabla \phi_s|_{x=L_n} = \nabla \phi_s|_{x=L_n+L_{\text{sep}}} = 0. \tag{4}$$

Mass conservation in the electrolyte phase

The mass conservation equation in the electrolyte phase is given by

$$\varepsilon_{\mathrm{l}} \frac{\partial c_{\mathrm{l}}}{\partial t} + \nabla \cdot \left(-D_{\mathrm{l,eff}} \nabla c_{\mathrm{l}} + \frac{i_{\mathrm{l}} t_{+}}{F} \right) = - \sum_{m} \frac{\nu_{\mathrm{Li+,m}} i_{\mathrm{v,m}}}{F}, \tag{5}$$

where,
$$i_{\mathrm{l}} = -\sigma_{\mathrm{l,eff}} \nabla \phi_{\mathrm{l}} + \left(\frac{2\sigma_{\mathrm{l,eff}} RT}{F} \right) \left(1 + \frac{\partial ln f}{\partial ln c_{\mathrm{l}}} \right) (1 - t_{+}) \nabla ln c_{\mathrm{l}} . \tag{6}$$

Boundary conditions are assigned as

$$-D_{\mathrm{l,eff}} \nabla c_{\mathrm{l}}|_{x=0} = -D_{\mathrm{l,eff}} \nabla c_{\mathrm{l}}|_{x=L}. \tag{7}$$

Charge conservation in the electrolyte phase

The charge conservation equation in the electrolyte phase

$$\nabla . i_{\mathrm{l}} = i_{\mathrm{v,total}} + Q_{\mathrm{l}}, \tag{8}$$

where,
$$i_{\mathrm{l}} = -\sigma_{\mathrm{l,eff}} \nabla \phi_{\mathrm{l}} + \left(\frac{2\sigma_{\mathrm{l,eff}} RT}{F} \right) \left(1 + \frac{\partial ln f}{\partial ln c_{\mathrm{l}}} \right) (1 - t_{+}) \nabla ln c_{\mathrm{l}}. \tag{9}$$

Note: Q_{l} is an additional source term which is 0 in our case.

Boundary conditions are given as

$$-\sigma_{\mathrm{s,eff}} \nabla \phi_{\mathrm{s}}|_{x=0} = -\sigma_{\mathrm{s,eff}} \nabla \phi_{\mathrm{s}}|_{x=L}. \tag{10}$$

Kinetics of electrochemical reaction

The kinetics of the electrochemical reaction can be given by the Butler-Volmer equation as

$$i_{\mathrm{Li}} = i_0 \left(\exp\left(\frac{\alpha_{\mathrm{n/p}} F}{RT} \eta \right) - \exp\left(-\frac{(1-\alpha_{\mathrm{n/p}}) F}{RT} \eta \right) \right). \tag{11}$$

Kinetics of the parasitic SEI formation reaction

In addition to the main graphite-lithium intercalation reaction on the negative electrode, the model considers parasitic SEI formation reaction as well. Ekström and Lindberg [53] formulated the kinetic expression for the SEI formation. The authors have reported the fitting of model parameters, using a lumped 0D model, to the experimental data during cycling for various states-of-charge. Additionally, only the graphite aging effects were considered in this work. The kinetics of the parasitic reaction is given by the following kinetic expression for the local current density, $i_{loc,SEI}$ in the negative graphite electrode.

$$i_{\mathrm{SEI}} = -(1 + HK)\frac{Ji_{\mathrm{loc,ref}}}{\exp\left(\frac{\alpha\eta_{\mathrm{SEI}}F}{RT}\right)+\frac{q_{\mathrm{SE}}fJ}{i_{\mathrm{loc,ref}}}}. \qquad (12)$$

Detailed definitions of symbols and further model descriptions are given elsewhere [53]. Tables 1 and 2 list the subscripts used in the P2D model equations and the important parameters, respectively.

Table 1. List of subscripts for the P2D model

Name	Description
s	Solid phase
l	Electrolyte phase
n	Negative electrode
sep	Separator
p	Positive electrode
app	Applied

m	Reactions under the porous electrode node

Table 2. List of important parameters for the P2D equations

Parameters	Description
D_{s}	Diffusivity of Li-ions in solid phase
r_{p}	Distance of the surface of the particle to the center(radius)
$\sigma_{\mathrm{s}}^{\mathrm{eff}}$	Effective conductivity in solid phase
$\sigma_{\mathrm{l}}^{\mathrm{eff}}$	Effective conductivity in the electrolyte phase
I_{app}	Applied current
ε_{l}	Porosity (electrolyte phase volume fraction)
$D_{\mathrm{l,eff}}$	Effective diffusion coefficient of Li-ion in the electrolyte phase
A	Electrode plate area
L	Length of the cell
t_{+}	Transference number of Li-ion (depends on the material of electrolyte)

i_{Li}	Kinetic current from charge-transfer reaction (Butler-Volmer kinetics)
$\alpha_{\mathrm{n\,/p}}$	Charge transfer coefficient for NE/PE
η	Overpotential
i_0	Exchange current density
L_{n}	Length of the negative electrode
L_{sep}	Length of the separator
L_{p}	Length of the positive electrode

It is assumed that the SEI formation is limited by a diffusion process through the formed SEI film, with the result that the aging slows down the thickening of the film. In normal operating conditions, the cell is subjected to a continuous charge/discharge load. Consequently, heat generation takes place within the cell due to various electrochemical processes. The thermal characteristics, such as heat generation due to various electrochemical reactions, in the case of the TR event can be described by the general energy conservation equation for both phases (solid and fluid) in the vector form as [51]

$$\rho C_{\mathrm{p}} \frac{\partial T}{\partial t} + \rho C_{\mathrm{p}} \mathbf{u} \cdot \boldsymbol{\nabla} T + \boldsymbol{\nabla} \cdot \mathbf{q} = \dot{Q}_{\mathrm{gen}}, \tag{13}$$

where,

$$\mathbf{q} = -k\, \boldsymbol{\nabla} T. \tag{14}$$

Here, k, is the thermal conductivity of the battery. It takes the form of a symmetric positive-definite tensor (matrix) and is given as

$$k = \begin{bmatrix} k_{\text{th}} & 0 & 0 \\ 0 & k_{\text{in}} & 0 \\ 0 & 0 & k_{\text{in}} \end{bmatrix}, \quad (15)$$

where, k_{in} being the in-plane thermal conductivity and k_{th} being and the through-plane thermal conductivity of the cell. In Eq. (3), ρ denotes the average density of the cell; C_{p} is the average specific heat capacity; T is the temperature; and $\dot{Q}_{\text{gen}}$ is the volumetric heat generation rate (HGR). The HGR of the cell is given by [54]

$$\dot{Q}_{\text{gen}} = \dot{Q}_{\text{elec}} + \dot{Q}_{\text{SEI}}, \quad (16)$$

where, $\dot{Q}_{\text{elec}}$ is the dominant HGR from the fundamental electrochemical reactions and $\dot{Q}_{\text{SEI}}$ is the dominant HGR for the SEI decomposition reaction. The convection term is zero in the solid phase due to the lack of fluid motion in that phase. The total electrochemical HGR is determined by the sum of irreversible heat from Joule heating and activation losses and reversible heat from electrochemical reaction and is given by [54]

$$\dot{Q}_{\text{elec}} = -(\boldsymbol{i}_{\text{s}} \cdot \boldsymbol{\nabla}\phi_{\text{s}} + \boldsymbol{i}_{\text{l}} \cdot \boldsymbol{\nabla}\phi_{\text{l}}) + \sum_{\text{m}} a_{\text{v,m}} \left\{ \left(\phi_{\text{s}} - \phi_{\text{l}} - E_{\text{eq,m}}\right) i_{\text{m}} + T \frac{\partial E_{\text{eq,m}}}{\partial T} i_{\text{m}} \right\}. \quad (17)$$

The variables in the electrochemical HGR are the electrode current $\boldsymbol{i}_{\text{s,}}$ electrolyte current $\boldsymbol{i}_{\text{l,}}$ electrode potential ϕ_{s}, electrolyte potential ϕ_{l}, the equilibrium voltage for each reaction $E_{\text{eq,m}}$, local current due to an electrochemical reaction i_{m}, the active specific surface area $a_{\text{v,m}}$ and the change in equilibrium voltage with respect to the temperature for each electrode reaction $\frac{\partial E_{\text{eq,m}}}{\partial T}$. It is to be noted that the variables $\boldsymbol{i}_{\text{s}}, \phi_{\text{s}}, \boldsymbol{i}_{\text{l}}, \phi_{\text{l}}$ and i_{m} are calculated based on the P2D equations. As previously mentioned, multiple exothermic reactions can occur inside the battery that may trigger the TR event. When the battery is in operation under charge/discharge load, reversible and irreversible reactions take place inside the battery, which releases heat and causes the temperature to rise. Along with these reactions, the SEI-forming parasitic reactions also occur in the anode of

the battery. After a certain growth, the SEI undergoes a decomposition reaction, which is exothermic in nature and releases heat. The HGR due to the SEI decomposition reaction is given by [55]

$$\dot{Q}_{\mathrm{SEI}} = a_{\mathrm{e}} h_{\mathrm{SEI}} j_{\mathrm{SEI,d}}, \tag{18}$$

where, a_{e} is the active specific surface area; h_{SEI} is the specific enthalpy of the reaction and $j_{\mathrm{SEI,d}}$ represents the reaction kinetics of the SEI decomposition reaction. Detailed descriptions of the symbols and additional equations for the reaction kinetics and the corresponding degradation parameters are given elsewhere [55]. It should be noted that the SEI formation has been reported to be a complex mixture of compounds, such as LiF, Li_2CO_3, lithium ethylene dicarbonate ($(CH_2OCO_2Li)_2$, LEDC) and lithium alkyl carbonates ($ROCO_2Li$) [56]. During the decomposition process, these compounds may have their own series of reactions. However, due to the lack of appropriate kinetic and thermodynamic data associated with all these reactions, it is reasonable to assume one global rate-limiting step for the SEI decomposition process. The intense heat release from the SEI decomposition reaction escalates the temperature of the battery. This creates high-temperature hotspots inside the battery, whose location is completely stochastic. The appearance of such hotspots may occur due to local defects present within the structure of the battery. These local defects can form due to multiple reasons, e.g., deflected current collectors, non-uniform packing, delamination, presence of impurities in the anode/cathode, burrs on the tab [57]. Since modeling does not allow the formation of such hotspots automatically, these hotspots are introduced artificially within the battery at random locations and simulate the battery operation. These hotspots are directly associated with the degradation mechanism in consideration. The heat release from the degradation of the battery leads to self-heating of the battery in a short period of time and causes a thermal runaway to occur. In this work, the SEI formation/decomposition has

been considered as the major degradation phenomenon that leads to the TR. Additionally, the developed model is solved for the continuity and momentum equations, that are given elsewhere [58,59].

2.1.1.1 Model implementation

The mathematical model constitutes a multi-scale and multi-domain approach and is implemented in COMSOL Multiphysics [60]. The model uses an unstructured quadratic finite element mesh and the backward Euler scheme for time discretization purposes. The PARDISO (COMSOL, 5.6) solver for a finite element problem to solve the system of linear equations as well as for the initialization and the transient stages is used. For the simulations presented in this chapter, a cylindrical 18650 cell with NMC chemistry has been chosen, and a 3D model has been implemented. A Graphite negative electrode, an NMC811 positive electrode, and an electrolyte 3:7 Ethylene carbonate (EC): Ethyl methyl carbonate (EMC)BMS with a 1M $LiPF_6$ salt from the COMSOL material library have been selected. The model has been simulated with a user-defined condition that when the maximum temperature of the battery exceeds 400 K, the calculations should stop. This has been implemented as the battery will undergo rapid self-heating beyond this point in a short period of time and will eventually explode.

2.1.2 DL methodology for image classification and object detection

The following section is dedicated to the description of the proposed DL framework, and it is structured in two parts: first, the dataset preparation and preprocessing is discussed, followed by the implementation of DL models. The section related to the implementation of the DL model is further divided into two parts. First, the classification technique used to predict the TR from the thermal images obtained from the multiphysics modeling is explained. Next, the development of

the object detection technique used to identify the location of high-temperature hotspots has been introduced which eventually leads to thermal runaway.

2.1.2.1 Dataset preparation and preprocessing for classification/object detection task

Initially, simulated thermal images of the battery are collected as sequences of video frames during the battery operation. Such thermal images contain physical features related, for example, to the battery surface temperatures and the cooling airflow. For applying the ML techniques to predict the TR, the temperature is the main subject of discussion. From the simulation results, the thermal images of the battery are saved in a continuous-time interval of battery operation considering a defined time step. To use ML/DL for the task of classification, it is important to divide the images into different labels. As mentioned in the introduction, three labels for the classification task have been considered, namely, Safe, Critical, and TR, depending upon the maximum surface temperature of the battery. The extraction and partitioning of these images into various labels are made in such a way that each label contains the same or nearly the same number of images. This is due to the concept of a balanced dataset in ML. In any ML/DL problem, class imbalance [61] is a major problem, as it reduces the accuracy of the model, making the model biased towards the class having a higher number of images. Further details on the image collection are provided in the results and discussion section. The next task is to preprocess the extracted data. Image preprocessing involves formatting the images before they can be used for training. This involves certain operations but is not limited to orienting, resizing, and color corrections. For the purpose of data preprocessing, techniques such as image normalization [62] and image augmentation [63] are used. Image multiphysics is used to normalize the values of the pixels for each of the images in a uniform distribution [63]. Feeding the neural network with normalized images is very crucial, as this helps the gradient descent algorithm to converge faster. Modern

developments in deep learning models are largely related to a significant quantity and diversity in data. For improving the performance of DL models, large datasets are very crucial. However, it is very costly and tedious to acquire such vast quantities of image data. In the problem investigated in this work, a large number of simulated images could be collected imposing a sufficiently small time step; however, such an operation makes the simulation time much longer. Hence, I have used the image augmentation [62] technique that considerably increments the diversity of image data. For the generation of new image data, various techniques, such as changing the brightness and contrast, padding, cropping, adding noise, and horizontal flipping have been used in this work. Image augmentation involves changing the exact pixel values of the images, thus creating diversity in the data while preserving the concept of a balanced set. Moreover, this diversity of images makes the model robust and generalized towards new test data, thus helping in improving the model performance on the test images.

2.1.2.2 TR classification using convolutional neural network

Image classification [64] involves taking an input (a picture) and predicting a class label or a probability referring to the input of a particular class. Convolutional neural networks have taken a quantum leap in image recognition. In this work, CNNs are used to classify three labels, i.e., safe, critical, and TR, which are directly related to the physical problem.

Learning takes place through an iterative process known as training. There are two methods by which training can be performed. The first method is learning from scratch. Learning from scratch is building completely a new model or mixing parts of other models and perform the training from the first layer. The second method is transfer learning with fine-tuning. This method consists of applying a pre-trained DL model to a dataset of interest. Transfer learning helps users to overcome the need for huge amounts of new data. A model already trained on a particular task

will be able to manage a new but similar task with minimal data. Additionally, the process of training can be boosted by utilizing a pre-trained model. This can result in a more effective model. Transfer learning yields the best results when the datasets are similar to the ones that the model was already pre-trained. For completely different datasets, learning from scratch is preferable. Hence, training from scratch is performed as the dataset is unique compared to other large datasets used to pre-train models.

The CNN architectures employed are, VGG16, VGG19, ResNet18, ResNet34, ResNet50, ResNet101, DenseNet121, DenseNet201, EfficientNetB6, EfficientNetB7, and MobileNetV3, are pre-established models widely recognized in the field of computer vision. [65–67] VGG16 and VGG19 are 16- and 19-layer CNN architectures, respectively, widely employed in visual object recognition software research. Both networks process RGB images as input, featuring a sequential stack of convolutional layers with small receptive fields and max-pooling layers [68]. ResNet, or Residual Network, variants used include ResNet18, ResNet34, ResNet50, and ResNet101. These architectures leverage the concept of residual learning, incorporating residual connections to facilitate the training of deeper networks [69]. The increased depth enables superior performance across various classification tasks. This architecture utilizes shortcut connections that perform identity mapping, bypassing one or more layers. These skip connections help in propagating gradients throughout the network efficiently, allowing ResNet50 to achieve excellent performance with its 50 layers, substantially deeper than traditional networks without such mechanisms. Figure 3 shows a general schematic for VGG16, VGG 19, and ResNet50 architectures to showcase the various layers, such as convolution, max pooling, and full connected.

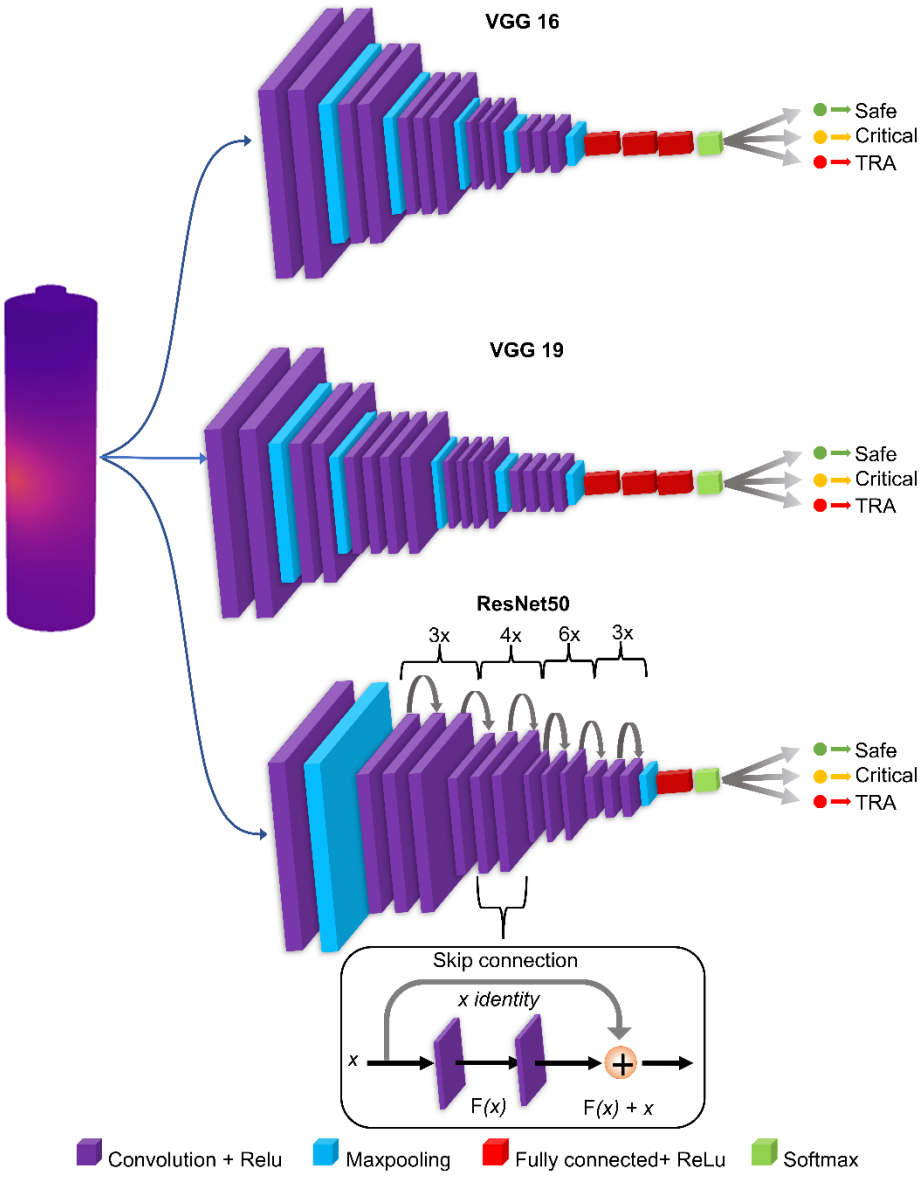

Fig. 3. A schematic illustration of the network architectures for VGG16, VGG19, and ResNet50, showing the input image of a battery and the corresponding labels. Additionally, the figure shows the skip connection for the ResNet50 network.

DenseNet121 and DenseNet201 are DenseNet architectures, where each layer receives input from all preceding layers [70]. Dense connectivity patterns contribute to efficient parameter usage, addressing vanishing gradient issues and enhancing overall model performance. The

EfficientNet family includes EfficientNetB0, EfficientNetB6, and EfficientNetB7, offering efficient scaling of depth, width, and resolution to achieve a balance between model size and accuracy [66]. These networks are particularly well-suited for resource-constrained environments. MobileNetV3 is part of the MobileNet family, designed for efficient deployment on mobile and edge devices [71]. It incorporates inverted residuals and linear bottlenecks for reduced computational cost, making it ideal for real-time applications. These models are well established and details of their network architecture can be readily found elsewhere [66,68–71]. Figure 4 shows a general schematic of DenseNet121, EfficientNet B0, and MobileNet V3 to showcase the various layers used for the purpose of feature detection and classification. The fundamental building blocks of DenseNet121 are dense blocks and convolution and max pooling layers. Dense blocks are where the direct connections between all layers are made, and within each block, each layer takes the concatenated outputs from all previous layers as its input, effectively reusing features throughout the network. Convolution and pooling operations help in reducing the dimensionality of the data, aiding in computational efficiency and reducing the risk of overfitting. EfficientNet B0 uses Mobile Inverted Bottleneck (MBConv) layers, which are a combination of depth-wise separable convolutions and inverted residual blocks. The MBConv layer is a fundamental building block of the EfficientNet architecture. The MBConv layer starts with a depth-wise convolution, followed by a point-wise convolution (1x1 convolution) that expands the number of channels, and finally, another 1x1 convolution that reduces the channels back to the original number. This bottleneck design allows the model to learn efficiently while maintaining a high degree of representational power. The architecture of MobileNetV3 is heavily influenced by the use of hardware-aware neural architecture search (NAS) techniques, which help to tailor the network design for optimal performance on specific hardware platforms. Additionally, it leverages

the latest developments from the research community, such as squeeze-and-excitation blocks and depthwise separable convolutions. These components are designed to enhance model efficiency by improving the representational capacity of the network per computational unit.

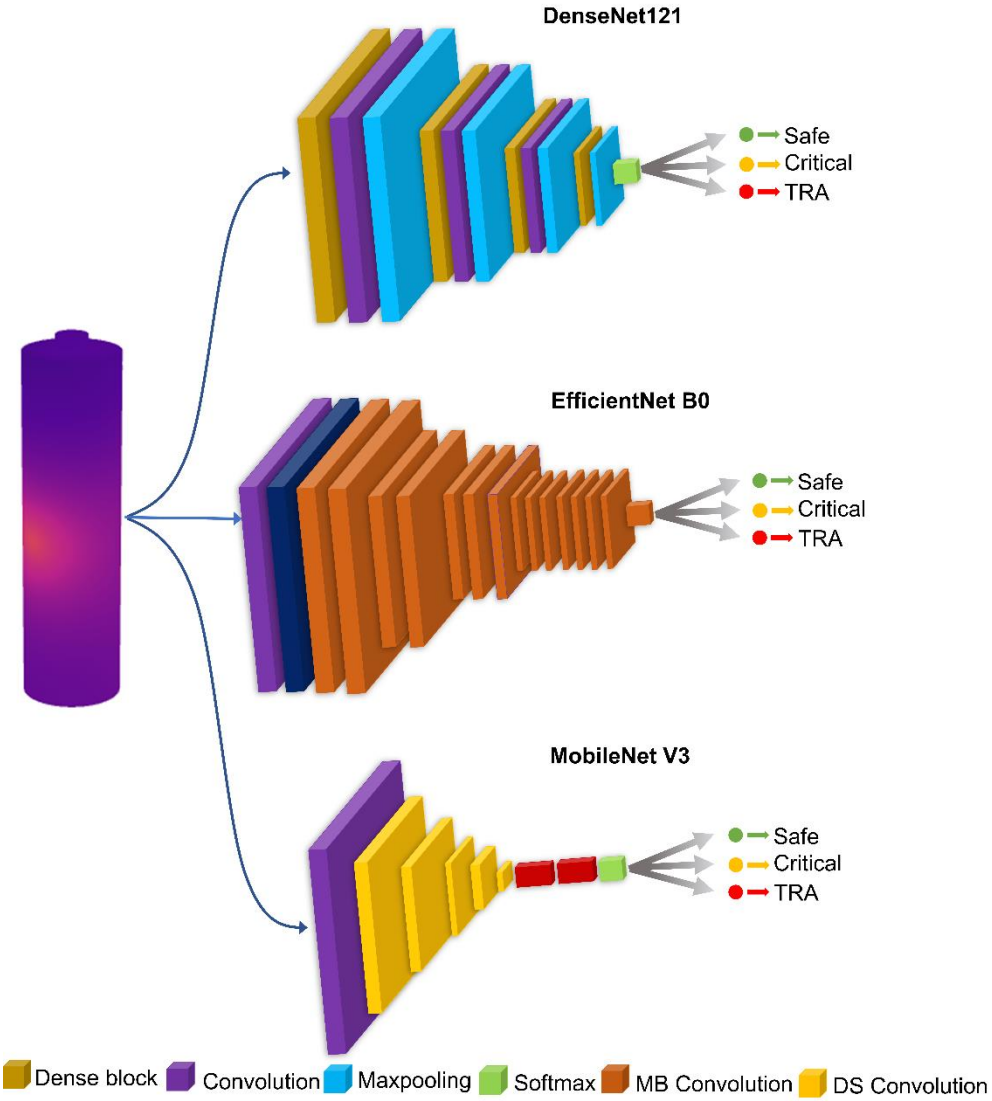

Fig. 4. A schematic illustration of the network architectures for DenseNet121, EfficientNet B0, and MobileNet V3, showing the input image of a battery and the corresponding labels.

2.1.2.3 Object Detection using YOLO

YOLO is an approach in the field of object detection using advanced DL algorithms. Here, object detection is performed as a regression problem, starting from the pixels of the image to the coordinates of the bounding box, to calculate the class probabilities [48]. Figure 5 shows a schematic illustration of YOLO network architecture. In this work, YOLO version 5 has been utilized for the purpose of object detection. The YOLO architecture begins with an input layer that takes battery thermal images as the initial data for the subsequent layers of the network. The core of YOLO consists of a backbone network comprising twenty-four convolutional layers, which are responsible for extracting hierarchical features from the input image. As these layers progress, they capture increasingly abstract and complex representations, allowing the model to discern intricate patterns in the visual data. Following the convolutional layers, YOLO integrates two fully connected layers that further process the extracted features, enhancing the network's ability to understand and interpret the visual information. YOLO also incorporates 1x1 reduction layers strategically within the architecture. These layers serve to reduce the dimensionality of the feature maps, optimizing computational efficiency while preserving critical information. Subsequent to the reduction layers, YOLO employs 3x3 convolutional layers. These layers play a crucial role in capturing spatial dependencies within the feature maps, facilitating the model's understanding of the spatial relationships between different elements in the image. The final stage of the YOLO architecture is the output layer, which produces a 7x7x30 tensor. This tensor represents the output of the detection layer of the network, with each cell in a 7x7 grid over the input image producing 30 predictions. Each prediction is a vector that contains the (x, y) coordinates of the center of a bounding box, the width and height of the bounding box, the confidence score (objectness score), and class probabilities for each of the classes the model is trained to recognize. These predictions

are encoded in the form of a tensor, and the information can be extracted and used to identify and locate objects within the input image. In essence, the YOLO architecture is carefully designed, progressing through convolutional backbones, fully connected layers, 1x1 reduction layers, and 3x3 convolutional layers. The final tensor output, structured as 7x7x30, efficiently encodes rich information for object localization and class predictions across the image grid. This detailed architecture empowers YOLO to excel in real-time and accurate object detection across a diverse range of datasets and scenarios.

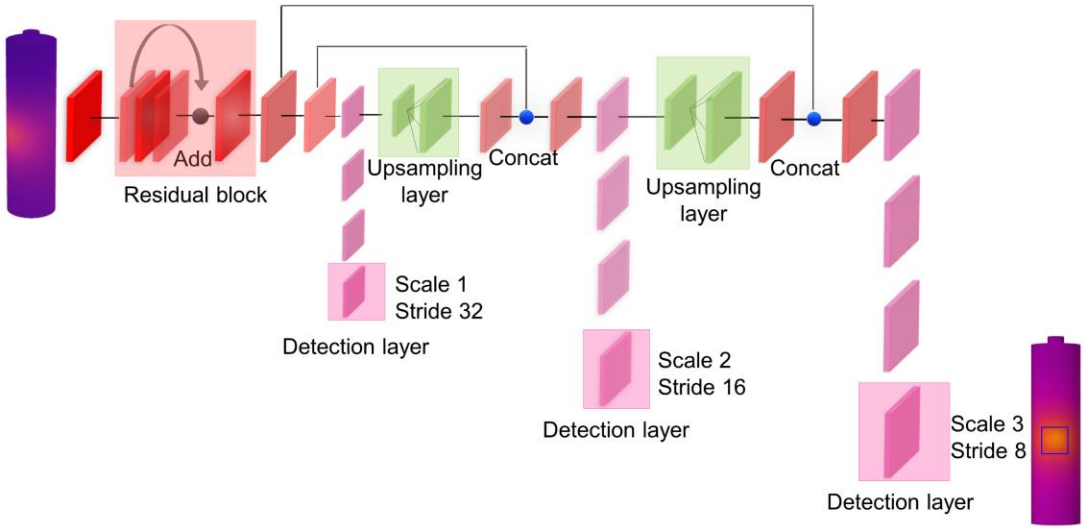

Fig. 5. A schematic illustration of the YOLO network architecture, together with the input image and its corresponding output available from the deep learning network.

2.2 Single cell thermo-electrochemical model results

This section discusses the results for the thermos-electrochemical model. It is challenging experimentally to observe the TR events in real-time. Moreover, during the battery preparation and its thermal treatment, a variety of side reactions could be triggered [72]. All these features

might potentially influence the propagation of the LIB's TR, causing some parts of the battery to be more susceptible to failures than others. Therefore, the exact modeling of the TR is not straightforward, considering the incomplete state of knowledge about the TR's associated events. For this reason, in the current modeling work, the locations of the TR hotspots are randomly chosen for cases with one and two hotspots. The schematic of the model containing a single hotspot along with the relevant boundary conditions is shown in Fig. 6. First, the multiphysics modeling results with one hotspot are presented, followed by the results for two hotspots, with the details of the effect of degradation on battery temperature and the capacity fade.

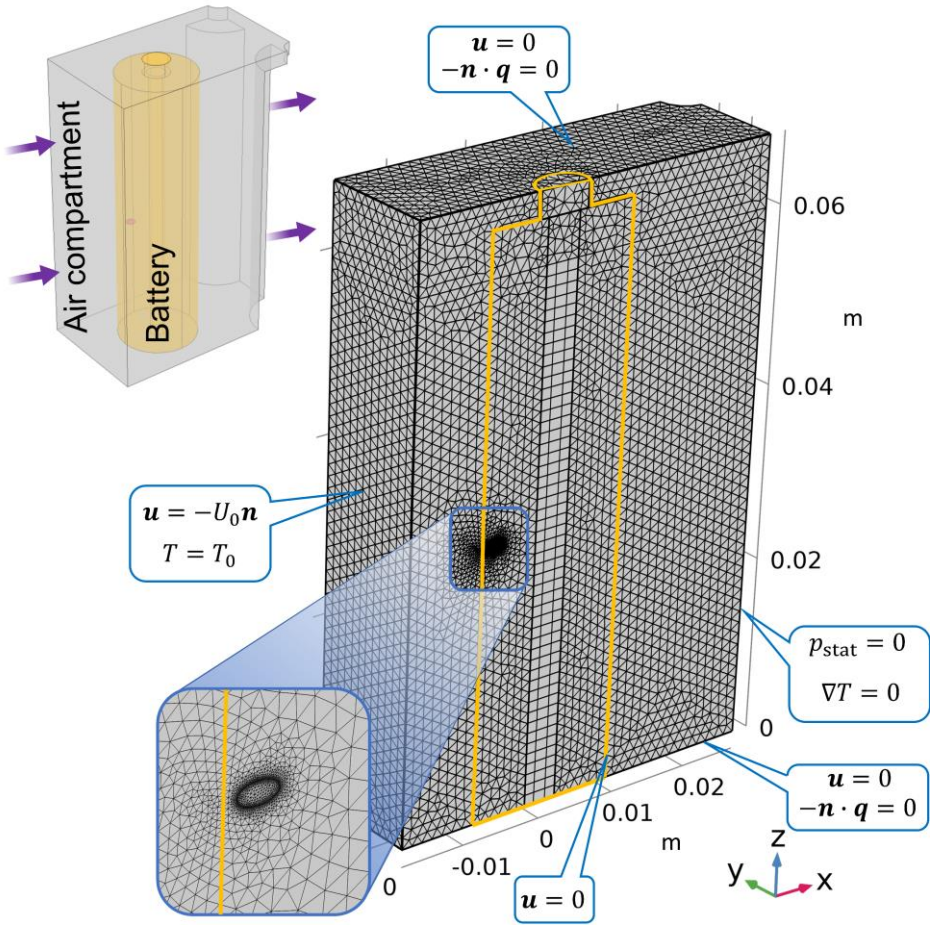

Fig. 6. Computational domain and mesh illustration for the multiphysics model with a zoom-in on the high-temperature hotspot showing all relevant boundary conditions for the 3D domain.

Before we dive into the TR modeling of cylindrical cells, I have first provided the validation of our developed electrochemical P2D model. The validation consists of the comparison between the discharge voltage characteristics obtained by the P2D model and the experimental data provided by the battery manufacturer. For this purpose, the discharge voltage for the first cycle of the model was compared directly against the experimental data at various discharge rates (cf. Fig 7a) and various temperatures (cf. Fig. 7b) [73]. Remarkably, the model exhibited a commendable alignment with the experimental data during the initial discharge cycle, substantiating the accuracy of the computational predictions. Significantly, the absence of observable degradation in the model during this initial discharge cycle prompted a targeted comparison with the corresponding experimental data, aiming to elucidate the essential dynamics in the early stages of battery operation.

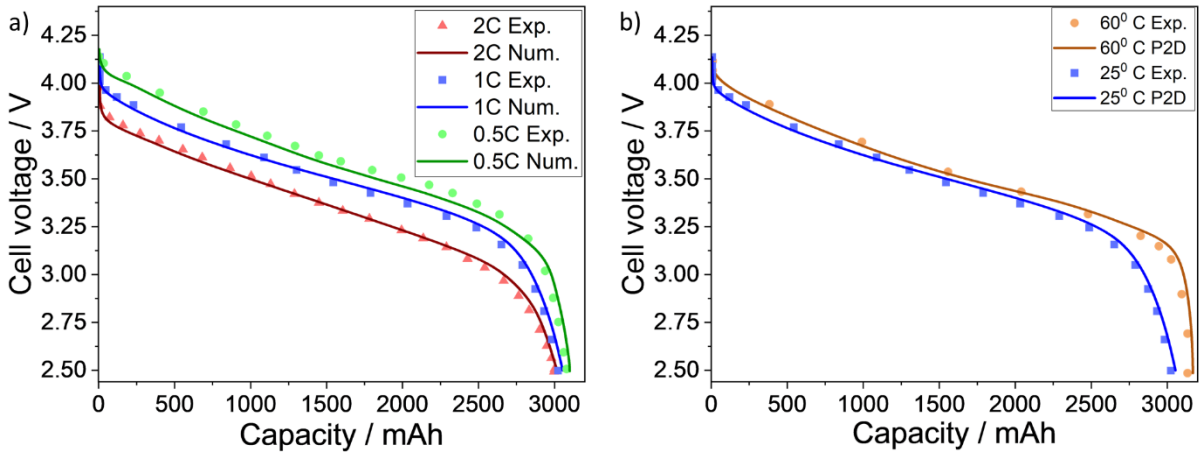

Fig. 7. Comparison of discharge characteristics for the P2D model (solid lines) and the experimental data (symbols) at different (a) C rates and (b) Temperatures (1C rate).

The developed model is used to investigate the effect of cell degradation on the temperature and battery capacity. For the simulation, a constant current/constant voltage (CCCV) charging is considered. Since, the current at which the voltage was validated is extremely small to initiate significant degradation, the cell is discharged at a 1C rate until it reaches a cut-off voltage of 2.5 V, followed by charging to 4.2 V. However, the heat release during this operation of the battery is observed to be sluggish, and the temperature rise is not sufficient for SEI decomposition to occur. Following this observation, the cell is discharged and charged at a 2C rate. Figure 8 shows the profile for charge and discharge curves pertaining to a single TR hotspot (cf. Fig. 8a), the change in the SEI thickness for one (red) and two (blue) TR hotspots, respectively (cf. Fig. 8b), and the rise in the maximum cell temperature of the battery for one (red) and two (blue) TR hotspots respectively (cf. Fig. 8c). Ideally, any battery needs large number of cycles to show prominent SEI growth, and the differences in the cycle-to-cycle behavior is usually assumed to be small. Hence, the SEI growth rate is accelerated by increasing the pre-exponential factor for proof of concept. This is a valid assumption for modeling purposes to observe the TR faster. Additionally, Fig. 8b illustrates the effect of the aging process on the growth of SEI formation. It is evident that the aging process slows down the rate of growth of SEI with time. Hence, I have considered the SEI formation to be limited by a diffusion process through the formed SEI film.

Figure 8 shows the reduction in the SEI thickness during discharge, implying the SEI decomposition reaction. As expected, a comparison between the temporal variations of the temperature in Fig. 8c indicates a more rapid temperature rise for the system with two TR hotspots. It should be mentioned that the model terminates after the stop condition is satisfied at 400 K, hence, the SEI does not completely decompose, as illustrated in Fig. 8b. SEI decomposition releases heat and increases the temperature of the battery. The exponential trend of the temperature

evolution, as seen in Fig. 8c, is explained by the Arrhenius relation of the SEI decomposition heat release [74]. This trend in the rise of temperature due to the degradation of the battery has been well reported in prior literature. Additionally, it was observed that the electrochemical HGR (cf. Eq. 7) was significantly lower in comparison to the heat release due to the degradation (SEI decomposition). Hanchard et al. [39] have devised a 1D model to estimate the variation of temperature during the TR event of LCO/graphite cells placed in a constant temperature oven during discharge and report similar temporal temperature profiles as in the results presented in this work(cf. Fig. 8). Kim et al. [75] have performed thermal abuse tests based on a 3D lumped model for the TR prompted by heating. The authors have reported the evolution of temperature to follow an exponential trend that is similar to the results shown in Fig. 8c. The introduction of hotpots would induce non-uniform temperature distribution inside the battery and, thus, non-uniform SEI generation. However, the SEI growth process has been implemented in the P2D model that assumes a uniform SEI growth for the negative electrode. The study of non-uniform SEI generation requires a 3D particle model in addition to a full-scale battery model and is subject to future work.

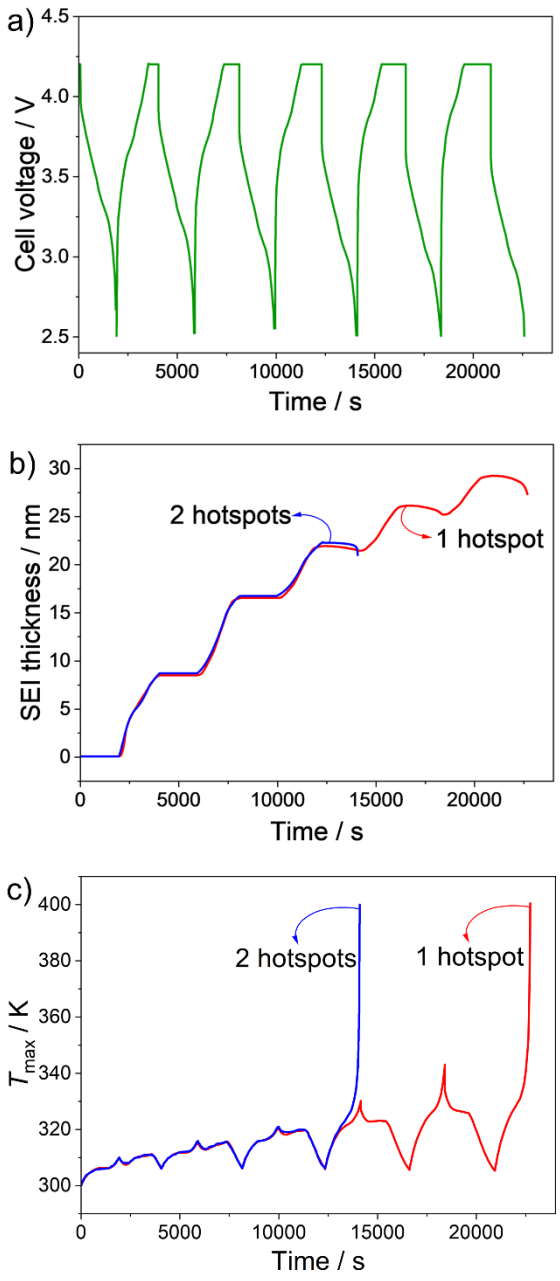

Fig. 8. Multiphysics modeling results illustrating the variation of general parameters relating to the electrochemical-thermal model with respect to time. (a) charge/discharge curves for one TR hotspot; (b) SEI thickness change for one (red) and two (blue) hotspots; and (c) Maximum temperature for the 18650 Li-ion battery.

Fig. 9 illustrates the total heat generation rate of the battery during operations for single (red) and two (blue) TR hotspots. At the beginning, both curves follow the same trend corresponding to the charge/discharge cycling. During the discharge, exothermic processes dominate, leading to the heat release, while the charging process is endothermic in nature causing some heat to be absorbed by the battery. The exponential heat generation rate is due to the SEI decomposition reaction, which leads the battery to the TR. The model containing a single hotspot contains a single Arrhenius function applied at that location, indicating the heat release due to the degradation of the battery, whereas the model with two hotspots contains two Arrhenius functions acting at the locations individually. Due to this reason, the sudden exponential heat release is observed sooner for the model with two hotspots as compared to the one with a single hotspot. A similar trend of heat release leading to the TR has been reported by Feng et al. [76] through experimental and modeling studies.

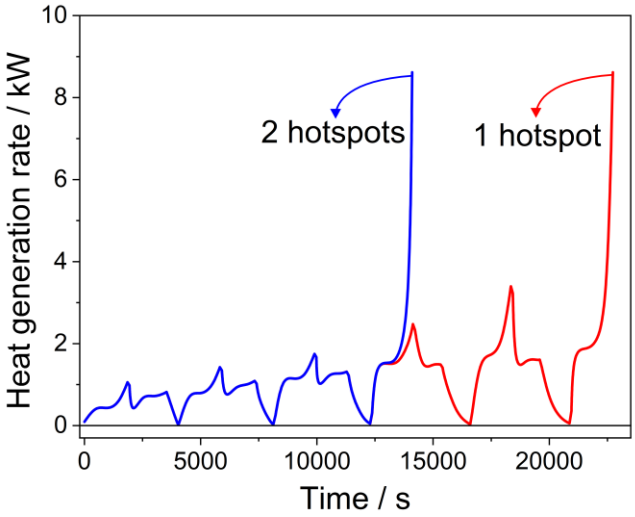

Fig. 9. Comparison of heat generation rates during the battery operation for the model with 1 hotspot (red) and 2 hotspots (blue).

The capacity fade can be observed in the discharge curves of graphite/NMC cell through operation for 2C charge/discharge, as shown in Fig. 10. The first discharge curve obtained from the simulations was directly compared to the datasheet provided by the battery manufacturer. It was observed that these results are in good agreement with the experimental test results [73]. Specifically, experimentally, the open circuit voltage of 4.2 V, along with the cut-off voltage of 2.5 V agrees well with the modeling results reported in Fig. 10. During the battery operation, the main contribution to the capacity fade is due to the cyclable loss of lithium-induced by the SEI formation. A shift is observed in the voltage curve at the end of the discharge. Additionally, as the number of cycles increase, the capacity tends to decrease, and the cut-off voltage is reached earlier.

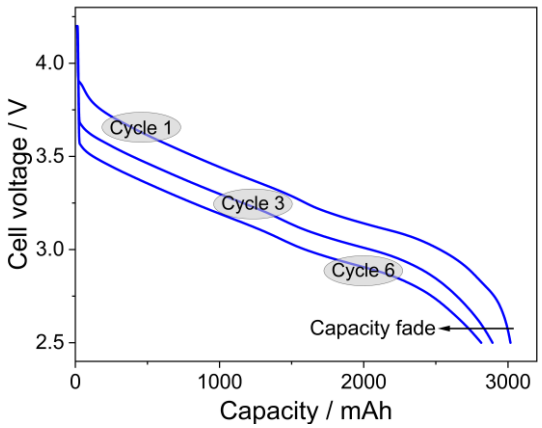

Fig. 10. Multiphysics simulation results for the cell voltage vs. the capacity of the cell in operation involving degradation of the battery showing results for 3 discharge cycles (cycle 1, cycle 3, and cycle 6).

This SEI formation-induced capacity fade has also been observed in experiments [77]. Ramadass et al. [78] and Lin et al. [79] have studied the degradation of different Li-ion cells and observed a shift in voltage. Additionally, they have reported that an SEI layer is formed on the surface of the negative electrode. The passive layer reduces the amount of cyclable lithium that,

leads to capacity fade with a shift in the potential. Accurate modeling of the TR is a challenging task. The objective during the model construction has been to extract thermal images of the battery, which provide a qualitative aspect of the TR initiation. The goal is to predict TR using ML on the thermal images extracted from simulations. The introduction of hotspots artificially within the battery for the initiation of the TR has already been mentioned. There could be multiple hotspots inside the battery depending upon the degradation mechanisms. The locations of these hotspots are completely random. Here, the number and locations of the hotspots has been varied within the battery to investigate the evolution of the cell temperature. Figure 11a shows the view of a battery for a constant 2C charge/discharge current with airflow velocity at the inlet being 0.1 m s^{-1}. It can be observed that due to the heat release from the SEI decomposition at the hotspot location, causes the temperature of the entire battery to rise and eventually lead to the TR. Figure 11b-11d shows the results for the battery temperature with cooling airflow for two high-temperature hotspots at different locations within the battery and the location is given with respect to the height of the battery (h_{batt}) and the radius of the battery (r_{batt}). Due to the heat release from the SEI decomposition reaction, other exothermic reactions are triggered, and this increases the temperature of the entire battery, triggering the TR event. Additionally, we observe distinct thermal behaviors when comparing scenarios with one versus two hotspots. The presence of two hotspots accelerates the thermal gradient development within the cell, underscoring a nonlinear escalation in risk factors leading to TR. This phenomenon is particularly evident in the rate of temperature rise (cf. Fig. 11c) and the spatial temperature distribution (cf. Fig. 11b-d). Our analysis provides crucial insights into the interplay of hotspot number and location, offering a comprehensive understanding of their impact on cell safety and performance.

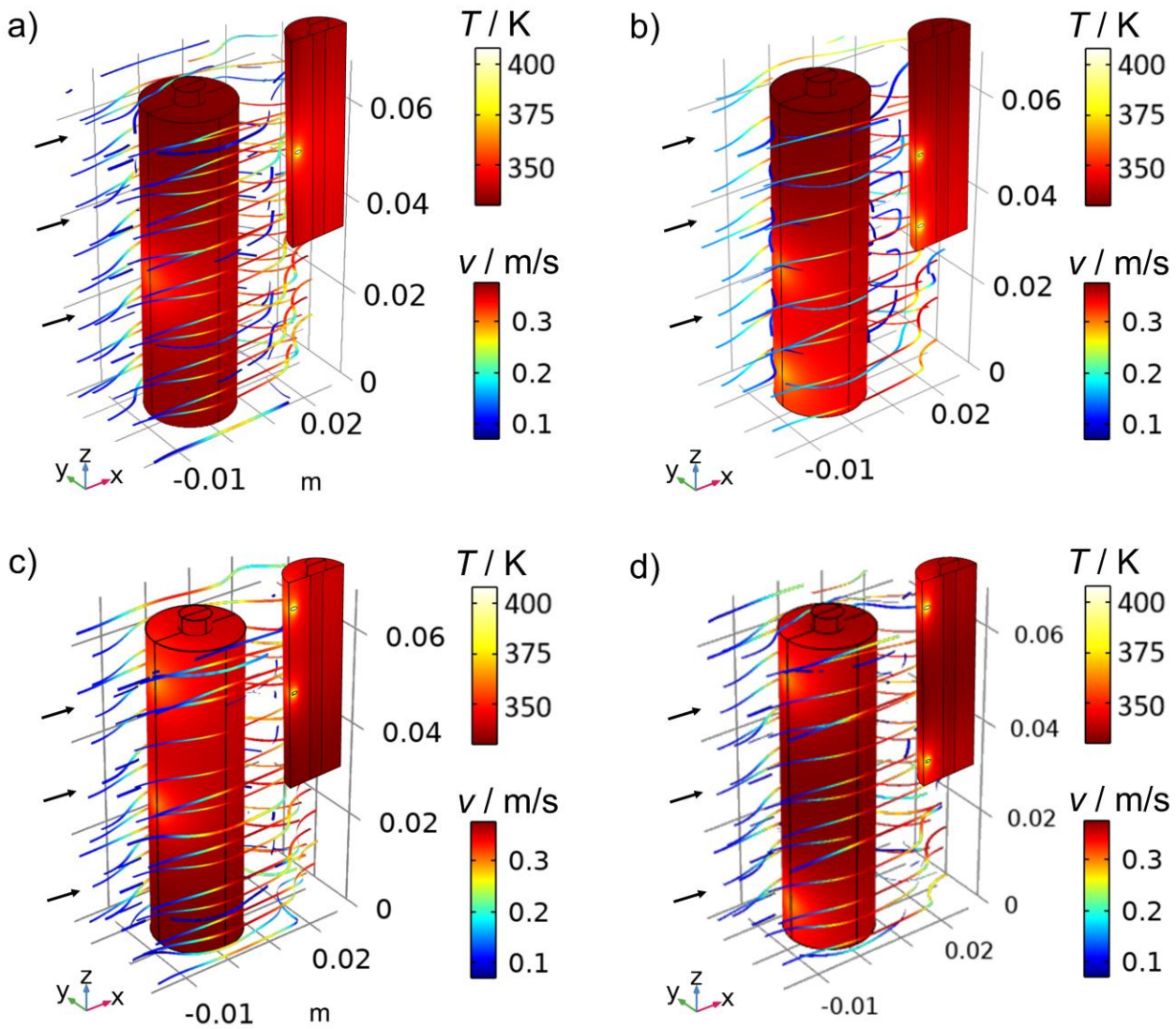

Fig. 11. Temperature distribution of the battery surface along with air cooling for single and two hotspots at 2C charge/discharge rate. A) Single hotspot, b) two hotspots at $\frac{h_{\text{batt}}}{6}$ mm and $\frac{h_{\text{batt}}}{2}$ mm from the bottom, c) two hotspots at $\frac{h_{\text{batt}}}{2}$ mm and $\frac{5h_{\text{batt}}}{6}$ mm from the bottom, and d) two hotspots at $\frac{h_{\text{batt}}}{6}$ mm and $\frac{5h_{\text{batt}}}{6}$ mm from the bottom. The figure shows the temperature for the battery and streamlines only represents the velocity magnitude for the cooling fluid. The velocity at the surface of the battery is zero due to the no slip condition.

2.3 DL for TR image classification and hotspot detection

DL enables a significantly broader scope of the study of LIBs. Many ML methods have shown to be extremely promising in the study of material properties in LIBs and the estimation of the state-of-charge (SOC) of a battery [18]. Due to these efficient applications, DL has received significant attention in recent years. Predicting TR events in batteries using DL is a relatively new approach. There are very few works in prior literature that use the idea of data-driven DL to forecast such events. Based on a thorough search of relevant literature, there is no work that uses an image-driven DL approach to forecast TR events, which is one of the novel aspects of this work. The multiphysics modeling results are taken as input to different DL techniques to identify and predict the TR. This section is divided into two parts. First, the results for the TR prediction as a classification task based on different DL architectures have been reported. Finally, the object detection technique, based on a regression approach, has been utilized to detect the high-temperature hotspots created within the battery at random locations due to the degradation mechanism.

2.3.1 Neural network based image classification

The TR classification requires the use of DL algorithms that learn to assign a class label to test data from the problem domain. To perform the task of classification, data preparation, and preprocessing is the most important step. For the data preparation step, images were collected and specified under a particular label based on the maximum temperature of the battery. When the maximum surface temperature is below 340 K, the images belong to the Safe class. The Critical class is defined when the maximum surface temperature is between 340 K to 370 K, also called the transition stage between the Safe and the TR regions. Finally, for temperatures greater than

370 K[80], the images are considered to belong in the TR class. To ensure an equal number of images for each label, the time at which the images were extracted from the multiphysics model played a vital role. During the simulation, the maximum battery temperature tends to be lower than 340 K for a long period of time due to the normal operation for the initial cycles, hence for this case, the time step is 100 seconds. For the transition phase between the safe and the TR region, i.e., the critical stage, the time step size is taken to be 10 seconds due to the process being fast. Finally, for the TR stage, which happens rapidly, the time step size is taken to be 1 second, ensuring an equal number of images extracted for each class of the DL model. This resulted in the collection of 1200 images, with each class having 400 images, respectively. This is the size of the entire dataset. The next step is data preprocessing, where the images are preprocessed using various techniques that have been discussed in the methodology section. Following this partitioning, the next task involved the splitting of the data into training, validation, and test sets, where the training set is fed as input to the model, and the validation set is used to evaluate the performance of the model during training. The training set contained 80% of the total number of images in the entire dataset, whereas the validation and the test sets contained 10%, respectively.

The training is performed over 300 epochs for each of the networks used. Additionally, a study was performed to observe the effect of different hyperparameters on the overall model accuracy using all the networks individually. For this purpose, batch size, optimizer and the learning rate were chosen to be varied and optimized. Batch size [81] is one of the most important hyperparameters to tune in modern DL systems. Larger batch size is mostly preferred as this gives the model the opportunity to look at larger data at any instant of training. The downside of a higher batch size is its high computational memory usage and higher training time. Here, the batch size varied as 8, 16, 32, and 64 and training was performed for the same number of epochs. Comparing

the accuracies for batch sizes of 32 and 64 gives the best results for all the networks taken into consideration, with the latter giving a slightly higher accuracy at the cost of much higher training time and memory usage. For this reason, a batch size of 32 was chosen. After optimizing batch size, the next important hyperparameter, i.e., the learning rate, was varied. In ML, the learning rate stands as a configurable parameter within optimization algorithms [82]. It plays a pivotal role in dictating the size of each step taken during iterations as the algorithm progresses towards minimizing a loss function. Symbolizing the degree to which recently acquired information supersedes prior knowledge, the learning rate serves as a metaphorical indicator of the swiftness with which an ML model assimilates new insights. Hence, optimizing the learning rate becomes very crucial. The learning rate was varied across different values of 0.01, 0.001, 0.0001, and 0.00001. The learning rate of 0.00001 yielded a slightly higher accuracy compared to 0.0001 at the cost of significantly longer training times. Therefore, a learning rate of 0.0001 was selected as the final value. Following the optimization of the batch size and the learning rate, the choice of optimizer was varied. Optimizers refer to algorithms or techniques employed to diminish the loss function or enhance production efficiency. These mathematical functions are contingent upon the learnable parameters of a model, namely the weights. Optimizers play a crucial role in determining the adjustments to the weights and learning rate of a neural network, aiding in the reduction of losses. Three popular optimizers – Stochastic Gradient Descent (SGD), Adam, and RMSprop – were considered for the purpose of optimizer tuning [83]. It was revealed that the Adam optimizer delivered the best results, and thus, it was selected as the final optimizer. Following the tuning of hyperparameters, then the optimized models were trained and tested on the test dataset. Estimation of the essential statistical parameters is necessary for assessing the performance of the model for the classification task. In a classification problem, to evaluate the performance of the model

effectively, I calculated the accuracy [84], precision [84], recall/sensitivity [84] and F1-score [84] for each and every class of the TR problem. Additionally, I computed the confusion matrix to monitor the model's performance in each class. Accuracy is the fraction of the correctly predicted images with respect to the total number of images (correct predictions and wrong predictions). Accuracy is given as

$$\text{Accuracy} = \frac{\text{TP+TN}}{\text{TP+TN+FP+FN}}, \tag{19}$$

where, TP denotes true positive, referring to the outcome when the model correctly predicts the positive class; TN denotes true negative, referring to the outcome when the model correctly predicts the negative class; FP denotes false positive, referring to the outcome when the model incorrectly predicts the positive class, and FN denotes false negative referring to the outcome when the model incorrectly predicts the negative class. In reference to the physical problem investigated in this work, TP can be understood as an image that has been correctly predicted in the TR stage. Similarly, FP for the TR stage is an image of a critical or safe stage but has been incorrectly predicted as the TR stage. Finally, FN can be understood as an image in the TR stage but has been incorrectly predicted as a safe or critical stage. Thus, FN is very critical for the TR problem as it means that the model is unable to detect an upcoming danger. The precision metric gives the proportion of positive identifications that were actually correct. It is defined as

$$\text{Precision} = \frac{\text{TP}}{\text{TP+FP}}. \tag{20}$$

Recall/sensitivity can also be referred to as the True Positive Rate (TPR). It gives the proportion of true positives that were correctly identified and is defined as

$$\text{Sensitivity} = \frac{\text{TP}}{\text{TP+FN}}. \tag{21}$$

The F1 score is also called as F-score or F-measure. It is determined by the weighted average of the recall and precision. It is defined as

$$\mathrm{F1} = 2 \cdot \frac{\mathrm{precision} \cdot \mathrm{recall}}{\mathrm{precision} + \mathrm{recall}}. \quad (22)$$

The complete list of values for accuracy, precision, recall, and F1 score is reported in Table 3. Upon analyzing the results presented in Table 3, it becomes evident that EfficientNetB7 outperforms its counterparts in terms of accuracy, recall, and F1 score. This finding signifies the superior efficacy of EfficientNetB7 in accurately predicting the class labels of images within the test dataset. Notably, the recall value for EfficientNetB7 stands out as notably higher compared to other networks, a critical aspect given its implication for safety considerations. A high recall value indicates a more precise identification of positive instances, a paramount factor in scenarios where misclassifying images with the TR label could lead to disastrous outcomes. The commendable performance of EfficientNetB7, as indicated by the elevated values of these performance metrics, suggests its potential extension to images derived from experimental data. Moreover, the high values of the performance metrics indicate that this idea can also be well extended to images collected from experimental data and could significantly help in predicting real-time TR detection in batteries.

Table 3. Performance of the networks used based on the most important performance metrics

Deep learning architecture	Accuracy	Precision	Recall	F1-score
VGG16	0.96	0.89	0.88	0.95
VGG19	0.96	0.98	0.87	0.96
ResNet18	0.91	0.88	0.91	0.89
ResNet34	0.95	0.92	0.93	0.95
ResNet50	0.98	0.95	0.95	0.97
ResNet101	0.98	0.96	0.97	0.97
DesneNet121	0.95	0.91	0.93	0.92
DenseNet201	0.96	0.93	0.95	0.96
EfficientNetB0	0.93	0.90	0.91	0.92
EfficientNetB6	0.99	0.94	0.96	0.97
EfficientNetB7	0.99	0.97	0.98	0.96
MobileNetV3	0.93	0.90	0.91	0.90

Figure 12 shows the confusion matrices for the best model for each group of networks considered. For instance, among the VGG group, the confusion matrix for VGG19 has been reported. Using a similar idea, confusion matrices of ResNet101, DenseNet201, EfficientNetB7 and MobileNetV3 are reported. This approach would provide qualitative and quantitative insights about the performance and robustness of different types of networks to the given problem rather than just comparing between the same type of networks with different layers. Since this is a three-label classification problem, the matrices are 3×3 in dimension. Here, the diagonal elements

represent the number of images that are rightly classified according to their true labels. The off-diagonal elements represent the number of miss-classifications for each label. Considering the first confusion matrix for VGG19, as shown in Fig. 12a, there are a total of 5 miss-classifications, all belonging to the same label. Among the 40 images, 35 of them are correctly classified, and among the five misclassifications, one image is misclassified as safe, and other four images are misclassified as TR. Figure 12b shows the confusion matrix for ResNet101. There are only two misclassifications for this network. Here, one image is misclassified as Critical while being in Safe and other one as Safe while being in Critical. Figure 12c shows the confusion matrix for DenseNet201, having 5 misclassifications out of 120 images in total. 2 images in the Safe label are misclassified as Critical, another 2 images in the Critical label are misclassified as Safe. Similarly, Fig. 12d shows the confusion matrix for EfficientNetB7, having no misclassifications. As the name goes, it is indeed the most efficient model for this problem. Finally, Fig. 12e shows the confusion matrix for MobileNetV3, showing the most number of misclassifications amongst the other models and it is also evident from Table 3 that reports the least accuracy for this model. Additionally, Fig. 12 shows a glimpse of the images for each of the cells in the confusion matrix, which provides a better visual representation and qualitative insight into the results obtained. Overall, it can be concluded that EfficientNetB7 performs the best among all the used DL methodologies.

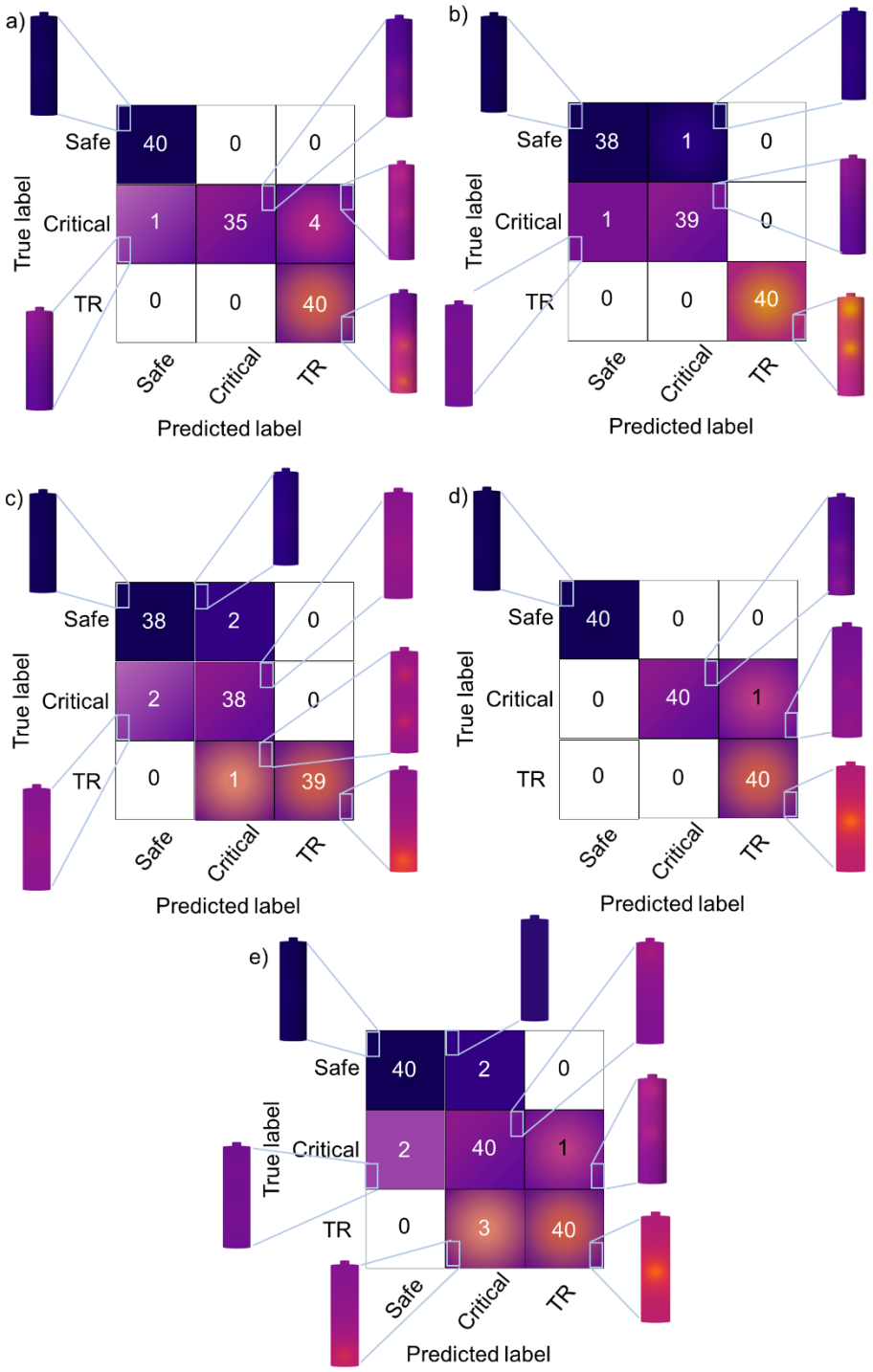

Fig. 12. Confusion matrix on the test dataset for different types of networks trained along with visualization of the images predicted for each label and their corresponding misclassifications: (a) VGG19, (b) ResNet101, (c) DenseNet201, (d) EfficientNetB7, and which MobileNetV3.

All three models exhibit good performances in predicting the labels accurately with minimal numbers of miss-classifications, which are acceptable from a statistical point of view. The test set is an unknown set, meaning the model has not previously seen it. A good performance on an unknown set signifies that the model is robust and has a good generalizing ability. The incorporation of scenarios with varying hotspot numbers significantly enhances the predictive robustness of our CNN models. The comparative analysis between single and dual hotspot situations reveals a marked improvement in the model's ability to discern complex thermal patterns, a key factor in predicting TR. This enhancement is quantified through improved accuracy and recall metrics in our models, indicating their heightened sensitivity to subtle variations in thermal imagery. These findings underscore the critical role of diverse training datasets in developing reliable predictive models for battery safety applications. Although the developed ML framework shows outstanding results in predicting thermal failures with great accuracy based on a single thermal image, there are certain challenges to extend it to a real battery module/pack due to its packaging, housing, etc. The results indicate the possibility for the application of various ML techniques to different views of a single cell and accurately predicting thermal failures. This approach can be well extended to the battery pack/module for effective prediction of thermal failures. It should be noted that using CNN with images can sometimes lead to 'fake warnings'. However, to mitigate this risk, a detail multiphysics model has been developed in this work, including SEI degradation to initiate TR. This model simulates realistic thermal images of batteries, providing diverse and realistic data for training various CNN architectures. Emphasizing rigorous training on a well-curated dataset, including multiple hotspots, further enhances the CNN's understanding of thermal behavior. Additionally, the methodology incorporates robust data preprocessing, rigorous validation, and hyperparameter tuning during the CNN training process.

This multifaceted approach not only improves the CNNs' predictive capabilities but also ensures their reliability in practical applications.

2.3.2 Deep neural network based hotspot detection

Object detection is a technique in the field of computer vision that helps to identify and track objects in a video or image [85]. Object detection can be utilized for effectively counting objects in a scene and determine their precise locations, along with accurately labeling them. Here, this technique to predict TR events in LIBs is applied. Figure 13 shows some predictions (output of network) of YOLO on different thermal images of batteries obtained from the multiphysics model simulations. In Fig. 13, three different images of the battery are shown as the test data for input. These images contain single and double high-temperature hotspots at different locations. The results indicate the high efficiency of YOLO in predicting the regions of TR initiation/hotspots where the temperature is very high compared to the other regions of the battery. This idea can also be extended for real-time TR hotspot detection in experimental battery operation.

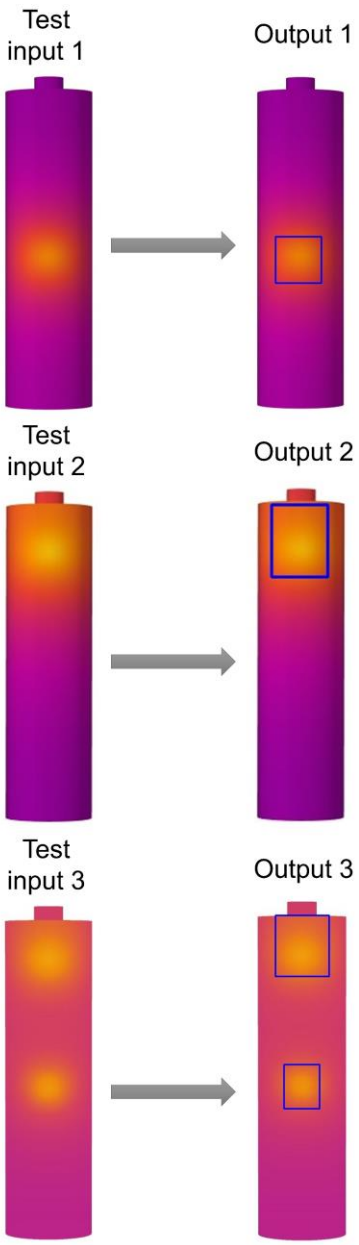

Fig. 13. Results for object detection technique showing different thermal images of the battery as input and its corresponding output containing bounding boxes over the high-temperature hotspots.

2.4 Summary and conclusion

A combined multiphysics model and DL-based framework has been developed for predicting the TR in cylindrical Li-ion batteries. This work contributes to the prevention of unfortunate events of the explosion of the battery operating devices (e.g., cell phones, EVs) in terms of both practical advances and improved fundamental understanding. The multiphysics model utilizes the COMSOL software to simulate the electrochemical-thermal nature of cylindrical battery type at various conditions. The thermal images of the battery obtained from the simulations are preprocessed for application in DL.

The ML/DL study is divided into two parts. First, a classification technique is used, which involves using CNNs for real-time prediction of the TR in the battery. Then, the YOLO (an object detection technique) is implemented and applied to the battery thermal images for the detection of the high-temperature hotspot zones. The performances of the DL classification algorithms and the object detection technique show great performance in the classification of the TR and predicting the location of the hotspots in the battery well. In the context of benchmarking thermal runaway classification, the selection of maximum temperature as a primary criterion is emphasized, reflecting its direct correlation with critical conditions leading to thermal runaway. The choice is grounded in the practical significance of maximum temperature as a clear and straightforward indicator of peak thermal stress experienced by the battery. This parameter provides a tangible and easily interpretable benchmark for distinguishing safe, critical, and thermal runaway states, aligning with the overarching objective of predicting and preventing thermal runaway in cylindrical Li-ion batteries. While acknowledging the importance of temperature rising rates in understanding thermal dynamics, prioritizing maximum temperature offers a pragmatic and actionable approach for assessing battery safety. The developed framework can be extended for

real-time TR hotspot detection and for practical battery operation. The main advantage of the proposed DL techniques is that they do not require the physical modeling of the internal battery chemistry, which is cumbersome in the TR scenario, rather, they rely only on the experimental/modeling data and the collected thermal images.

There are certain practical challenges associated with acquiring thermal images in real-world scenarios. However, the decision to incorporate thermal images as inputs for the ML modeling is based on their unique advantages, providing a comprehensive representation of spatial and temporal temperature variations within the battery. This approach enables early detection of potential issues and seamless integration with the multiphysics modeling methodology. While recognizing concerns about data storage, I can well argue that the benefits in predictive accuracy and safety outcomes justify the use of thermal images. With advancing technology facilitating the handling of large datasets, including thermal imaging data, making it increasingly practical to handle large datasets. Although this method of predicting battery failures seems a viable option towards ensuring the safety of electric vehicles, there are a few potential limitations in its practical implementation on a large scale. Firstly, the initial cost to setup might be significantly high. Secondly, the various types of degradation that are possible, along with more cell designs, should be considered as well. This would help in creating a larger dataset that would be more reliable than the present one. It must be noted that the developed multiphysics modeling and ML framework is generic and may be well extended to various Lithium-ion batteries with various geometric configurations and contrasting anode/cathode materials in addition to cylindrical cells.

CHAPTER 3. FRAMEWORK TO PREDICT THERMAL FAILURES IN ELECTRIC VEHICLES

This chapter discusses a novel approach by combined multiphysics simulation with ML for TR prediction in battery modules. Focusing on a liquid-cooled module with Panasonic 2170 cells, a representative unit of four cells is modeled due to computational constraints. The study considers SEI decomposition as a major degradation mechanism leading to TR. Additionally, the model incorporates artificially placed high-temperature hotspots within the battery at various locations to trigger TR. The batteries undergo two different load cycles: constant charge/discharge cycles and the Federal Test Procedure 75 (FTP 75) driving cycle to reflect realistic EV behavior. Addressing real-time challenges of temperature measurement, thermocouples are attached to the battery's surface in the multiphysics model, mimicking the real-life scenario of battery modules in standard EVs. Temperature data is extracted from these thermocouples at specific coordinates and time steps, creating spatio-temporal data for analysis. Traditional methods like autoregressive integrated moving average (ARIMA), its variants, or simple neural networks (NN) prove inadequate for mid- and long-term temperature prediction. To overcome this, a combined GNN-LSTM network is developed [86,87], leveraging temperature history from thermocouples to predict future spatiotemporal temperatures. This analysis aids in determining whether the battery will experience TR. The research contributes to a hybrid methodology, integrating physics-based modeling and data-driven ML for effective TR prediction in battery modules.

3.1 Combined multiphysics and spatiotemporal ML-based methodology

This section describes the general workflow of the framework involving a combined multiphysics and ML-based approach for the prediction of TR. First, a computational approach to investigate the battery degradation using an electrochemical-thermal model of the LIB battery module representative unit is described. This is followed by the extraction of temperature from the thermocouples attached to the battery surface, after undergoing further data preprocessing steps. The details of the orientation of these thermocouples are provided in Fig. 14. Figure 14 shows the orientation of the thermocouples around a single battery. It should be mentioned that each battery is equipped with the same type of orientation. However, for illustration purposes, I have shown a single battery. These various orientations of the thermocouples were used to collect the temperature of the battery at different spatial coordinates and at different time steps. This data was then used to prepare the dataset for the machine learning study.

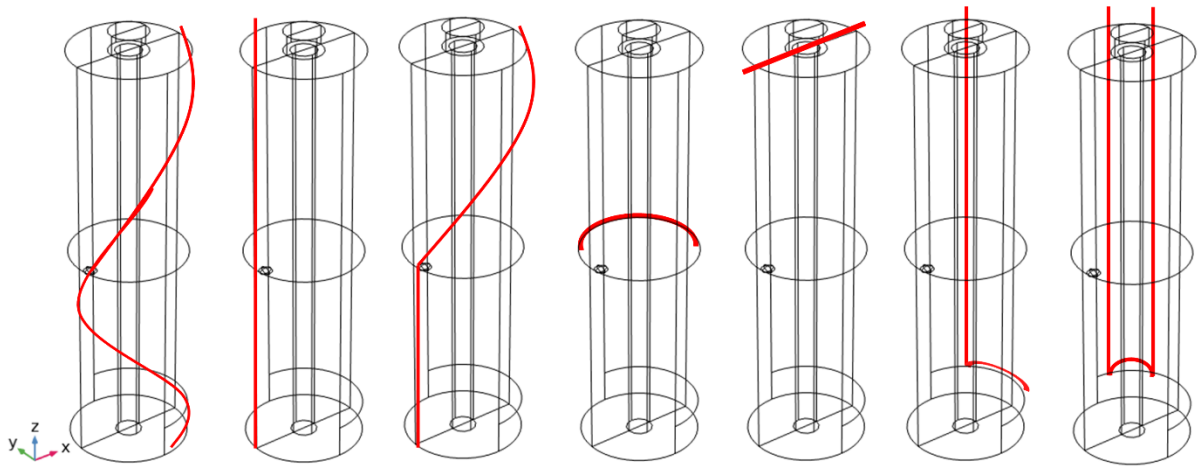

Fig. 14. Schematic illustration of the various thermocouples attached to a battery. Note: The picture shows thermocouples for only one battery

Then, the obtained data from the multiphysics calculations is fed into the developed ML algorithm featuring a GNN-LSTM network. This network predicts the future temperature of the

batteries based on the temperature history that was fed into the system. Based on such a temperature profile, the TR can be predicted and potentially stopped. Figure 15 shows the class of systems modeled in this work together with the ML workflow. In particular, the left segment of Fig. 15 illustrates the multiphysics model of a LIB module, which forms the basis for generating a dataset reflective of the battery's operational parameters. This dataset, containing thermal and electrochemical characteristics derived from the model, is then utilized by the ML algorithm, represented in the central part of the schematic. Multiphysics modeling is the three-dimensional representation of cylindrical LIB cells within a module, with a cooling snake placed between the cells. Subsequently, the central portion of the illustration of Fig. 15 describes the ML workflow, beginning with the thermocouple data represented by a red line around the cylindrical cell. This data is processed through various layers of the ML algorithm, including graph convolution and max pooling, which are instrumental in obtaining the spatial characteristics of the data. The temporal aspects are analyzed by the LSTM layer, which is adept at discerning patterns over time. The process concludes in a fully connected neural network layer that blends the spatial-temporal information to output a predictive model for TR.

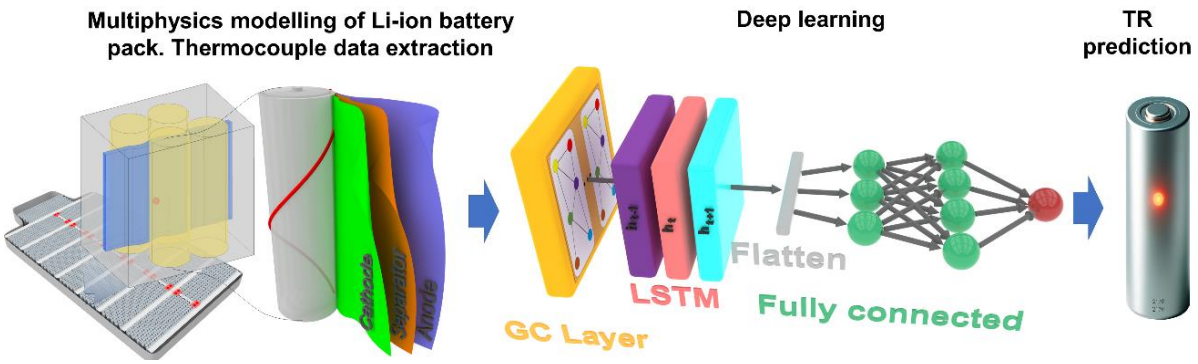

Fig. 15. Schematic illustration depicts a study that combines physics-based modeling and ML to predict and detect TR in cylindrical LIB modules. The left-hand side shows the multiphysics model used to generate the data set, which is then used in the ML model (middle image) to predict the occurrence of TR in LIBs. Note: the images on the left are not to scale, merely for illustration purposes.

3.1.1 Battery module multiphysics methodology

This section describes the methodology used in the multiphysics model. The general electrochemical model is discussed first, followed by the description of the thermal model. Additionally, details about the computational domain and the general introduction to the model implementation are discussed. The multiphysics model makes use of the FEM to simulate the electrochemical-thermal behavior of a cylindrical battery under various conditions. The electrochemistry is modeled using the P2D model [46–48], and the temperature of the batteries is simulated using a 3D model. The two models are then coupled by the generated heat source and the temperatures. A detailed description of the governing equations and corresponding boundary conditions related to the P2D model is provided in chapter 2. In addition to considering the main

graphite-lithium intercalation reaction on the negative electrode, the model also takes into account the parasitic solid electrolyte interphase (SEI) formation reaction in one of the batteries that is supposed to be under degradation and eventually triggers TR. The kinetic expression for the SEI formation reaction is based on the work of Ekstrom and Linderberg [49] and is provided in chapter 2. It is assumed that the SEI formation is limited by a diffusion process through the formed SEI film, resulting in a slowdown of the film thickening with aging. Under normal operating conditions, the cell is first subjected to a continuous charge/discharge load (i.e., constant C-rate), leading to heat generation within the cells due to various electrochemical processes. Subsequently, cells are subjected to the Federal Test Procedure (FTP) 75 driving cycle load, which simulates authentic vehicular and battery conditions to mirror real-world environmental influences. The thermal characteristics, including heat generation during a TR event, are described by the general energy conservation equation solved for essentially three domains, namely battery module representative unit where conduction is the dominant heat transfer mechanism (Eq. 23), the cooling snake assembly where convection dominates (Eq. 24) and finally the outer box which is a solid domain composed of the filler material where conduction is the main heat transfer mechanism (Eq. 25) [48]

$$\rho_b C_{\mathrm{pb}} \frac{\partial T_b}{\partial t} + \boldsymbol{\nabla} \cdot (-k_b \boldsymbol{\nabla} T_b) = \dot{Q}_{\mathrm{g}}, \tag{23}$$

$$\rho_l C_{\mathrm{pl}} \frac{\partial T_l}{\partial t} + \rho_l C_{\mathrm{pl}} \mathbf{u} \cdot \boldsymbol{\nabla} T_l + \boldsymbol{\nabla} \cdot (-k_l \boldsymbol{\nabla} T_l) = 0, \tag{24}$$

$$\rho_o C_{\mathrm{po}} \frac{\partial T_o}{\partial t} + \boldsymbol{\nabla} \cdot (-k_{\mathrm{o}} \boldsymbol{\nabla} T_o) = 0. \tag{25}$$

Here, k_b is the thermal conductivity coefficient of the battery. It takes the form of a symmetric positive-definite tensor (matrix) and is given as and is given by,

$$k = \begin{bmatrix} k_{\text{th}} & 0 & 0 \\ 0 & k_{\text{in}} & 0 \\ 0 & 0 & k_{\text{in}} \end{bmatrix}, \tag{26}$$

where, k_l and k_o are the average thermal conductivity coefficients of the cooling liquid and the filler material; ρ_b, ρ_l and ρ_o denote the average densities of the cells, cooling liquid and the filler material; $C_{\text{pb}}, C_{\text{pl}}$ and C_{po} are the average specific heat capacities of the cells, cooling liquid and the filler material; and $\dot{Q}_{\text{g}}$ is the volumetric heat generation rate for the battery. The heat generation rate of the cell under SEI degradation is given by [54]

$$\dot{Q}_{\text{g}} = \dot{Q}_{\text{e}} + \dot{Q}_{\text{SEI}}, \tag{27}$$

where, $\dot{Q}_{\text{e}}$ is calculated as the combined effects from the irreversible heat stemming from Joule heating and activation losses and the reversible heat resulting from electrochemical reactions. Further details about $\dot{Q}_{\text{e}}$ given in our previous work [88]. As stated earlier, the battery undergoes various exothermic reactions during its operation, which can lead to a TR event. During charging and discharging, reversible and irreversible reactions occur within the battery, causing the temperature to increase. Additionally, parasitic reactions take place in the anode of the battery, leading to the formation of SEI. When the SEI grows to a certain extent, it decomposes, releasing heat and causing temperature to rise further. The heat release due to the decomposition of the SEI layer is described by a modified Arrhenius function [39]. According to this function, the rate of the SEI decomposition reaction, and consequently the heat release, increases exponentially with temperature. This behavior is due to the fact that higher temperatures provide more energy to overcome the activation energy barrier for the decomposition reaction. The details of the SEI decomposition reaction, including its corresponding degradation parameters, symbols, and reaction kinetics, are provided elsewhere. [55] The exothermic reaction resulting from the decomposition of SEI in batteries significantly elevates the battery's temperature, giving rise to

randomly distributed hotspots within the battery. These high-temperature hotspots are stochastic in nature and can occur spontaneously due to local defects. Standard modeling techniques do not inherently incorporate these hotspots, necessitating their artificial placement in random locations within the battery during the model development process prior to simulations. These artificially introduced hotspots are specifically associated with the studied degradation mechanism, and their heat release induces self-heating of the battery, consequently triggering TR. The present investigation primarily focuses on the self-heating phenomenon induced by the formation and subsequent decomposition of SEI, which is regarded as the primary degradation process.

In the multiphysics modeling of the battery module with a cooling serpent, the heat dissipation involves concurrent conduction and forced convective heat transfer mechanisms. The cooling serpent, composed of a thermally conductive metal, establishes direct contact with the battery cells, facilitating efficient conduction of heat from the battery to the serpent's surface. This conduction pathway ensures a direct and prompt transfer of thermal energy. Simultaneously, a liquid coolant circulates within the cooling serpent under forced convection conditions along with the assumption of a laminar flow, driven by a specified inlet velocity. The forced convection scenario enhances the convective heat transfer process, as the liquid coolant actively carries away the absorbed heat. The value of the Reynolds number calculated for the flow was 142, which implies laminar flow and simplifies the fluid dynamics in our model, providing a practical and computationally manageable approximation while retaining the key features of heat transfer. This combined conduction and forced convective model within the multiphysics framework offers valuable insights into the thermal behavior of the battery module. While the detailed description of the Navier-Stokes equations is omitted for conciseness, this comprehensive approach captures the nuanced dynamics of heat transfer within the system. Additionally, proper boundary conditions

are required in order to solve the problem. Information regarding the initial and boundary conditions for the governing equations has been described in the Computational domain section. In EV battery systems, temperature sensors are meticulously attached to the surfaces of battery cells to precisely measure temperature fluctuations during operation. These sensors, crucial for monitoring the thermal health of the battery, provide real-time data that is essential for maintaining optimal performance and safety. As the battery undergoes charging and discharging cycles, the sensors detect any deviations from normal temperature ranges, allowing the BMS to adjust operational parameters accordingly. This might include modulating the charging rate or activating cooling systems to prevent overheating. The strategic placement of these sensors across the battery surface ensures comprehensive coverage, enabling the detection of hotspots or uneven temperature distributions that could indicate potential issues or inefficiencies within the battery pack. Through this vigilant thermal monitoring, EVs can achieve greater efficiency, longevity, and reliability of their battery systems, safeguarding the vehicle's performance and the user's safety. In order to mimic the temperature measurement and, eventually TR prediction in a model, I have artificially introduced certain curves on the surface of the batteries to represent a thermal sensor. The temperature of the battery is collected at different time steps and along various spatial coordinates of these specified curves. The orientation and shapes of these curves can have a wide range of possibilities. However, that number could be significant, hence, I have considered a range of possible orientations ranging from the helix, straight line and combinations as well, with the final objective to extract spatiotemporal temperature data to be fed into the ML algorithm, with the final objective to extract spatiotemporal temperature data to be fed into the ML algorithm.

3.1.1.1 Computational domain

This subsection is dedicated to the description of the computational domain and the related boundary and initial conditions for the multiphysics model. Figure 16 illustrates a computational domain created in COMSOL Multiphysics, depicting the electrochemical domain involving the P2D model (cf. fig. 16a) and a representative unit of a battery module consisting of four cylindrical cells arranged in alternating 2x2 configuration, with an integrated cooling snake assembly (cf fig. 16b). It should be noted that there is 1 P2D model for each of the batteries for the electrochemical problem. However, the domains are identical in geometry, hence, only a single figure has been shown for visualization purposes. The 3D domain is discretized using a finite element mesh. Each cylindrical cell, labeled B1 through B4, is in contact with the cooling assembly, indicated by the red zigzag lines, which is designed to dissipate heat away from the cells efficiently. The serpentine cooling configuration is a critical component in the thermal management of the battery module, ensuring uniform temperature distribution and mitigating the risk of TR. The unstructured mesh with quadratic elements is constructed to capture the complex geometry of the cells and the cooling assembly, with a finer resolution at critical areas to ensure accurate simulation results. The mesh density is increased near the interfaces between the cells and the cooling assembly to resolve the thermal gradients and fluid flow characteristics more precisely. Additionally, the figure shows the boundary conditions, which are further described below.

Given that the system operates based on electrochemical and thermal principles, it possesses two distinct sets of initial circumstances: one pertaining to electrochemical factors and the other related to thermal aspects and fluid movement. Regarding the electrochemical aspect, the initial state-of-charge (SOC) values are configured such that the negative electrode possesses a value of 0.99, while the positive electrode holds a value of 0.01. The battery commences with a

discharge cycle succeeded by a charging cycle, necessitating the negative electrode to exhibit the highest concentration of Li-ions and the positive electrode to possess the lowest concentration. Proceeding under this assumption, the initial Li-ion concentration in the negative electrode is denoted as $0.99 \times c_{\mathrm{s,neg\_max}}$, representing the maximum concentration achievable for the negative electrode. Similarly, the initial Li-ion concentration in the positive electrode is designated as $0.01 \times c_{\mathrm{s,pos\_max}}$, signifying the maximum Li-ion concentration attainable for the positive electrode. To maintain equilibrium in terms of electronic current, a potential of 0 V is imposed on the current collector of the negative electrode, while the specific value of the current is determined at the positive electrode's current collector. This model follows a cyclical pattern which the load current experiences a discharge stage, succeeded by a charging stage. Furthermore, the separator boundaries are electrically insulated to prevent electric currents. In order to preserve the charge balance within the electrolyte, the charge flux is set to zero at the current collector boundaries. Similarly, the mass flux of Lithium ions is assumed to be zero to preserve material balances. Additionally, the flux of Li ions is dictated by the rate at which the local electrochemical reaction occurs at the surface of the particle. In the thermal configuration of the coolant through the cooling snake assembly, the batteries are positioned within a casing with filler material, showcased in Fig. 16b. The inlet is designated with a temperature of 298 K, while at the outlet, the zero gradient temperature value is set. The external boundaries at the top and the bottom have been thermally insulated. The battery is assumed to have an initial temperature of 298 K. Furthermore, a fully developed flow has been assumed at the inlet and outlet of the cooling compartment. Periodic boundary conditions have been enforced for the side walls of the casing representing repeating units of battery and cooling snake assembly. The walls of the cooling snake are subjected to a no-

slip boundary condition. The temperature is continuous across the boundary of the batteries and the cooling snake. The temperature gradient is zero at the outlet of the cooling snake.

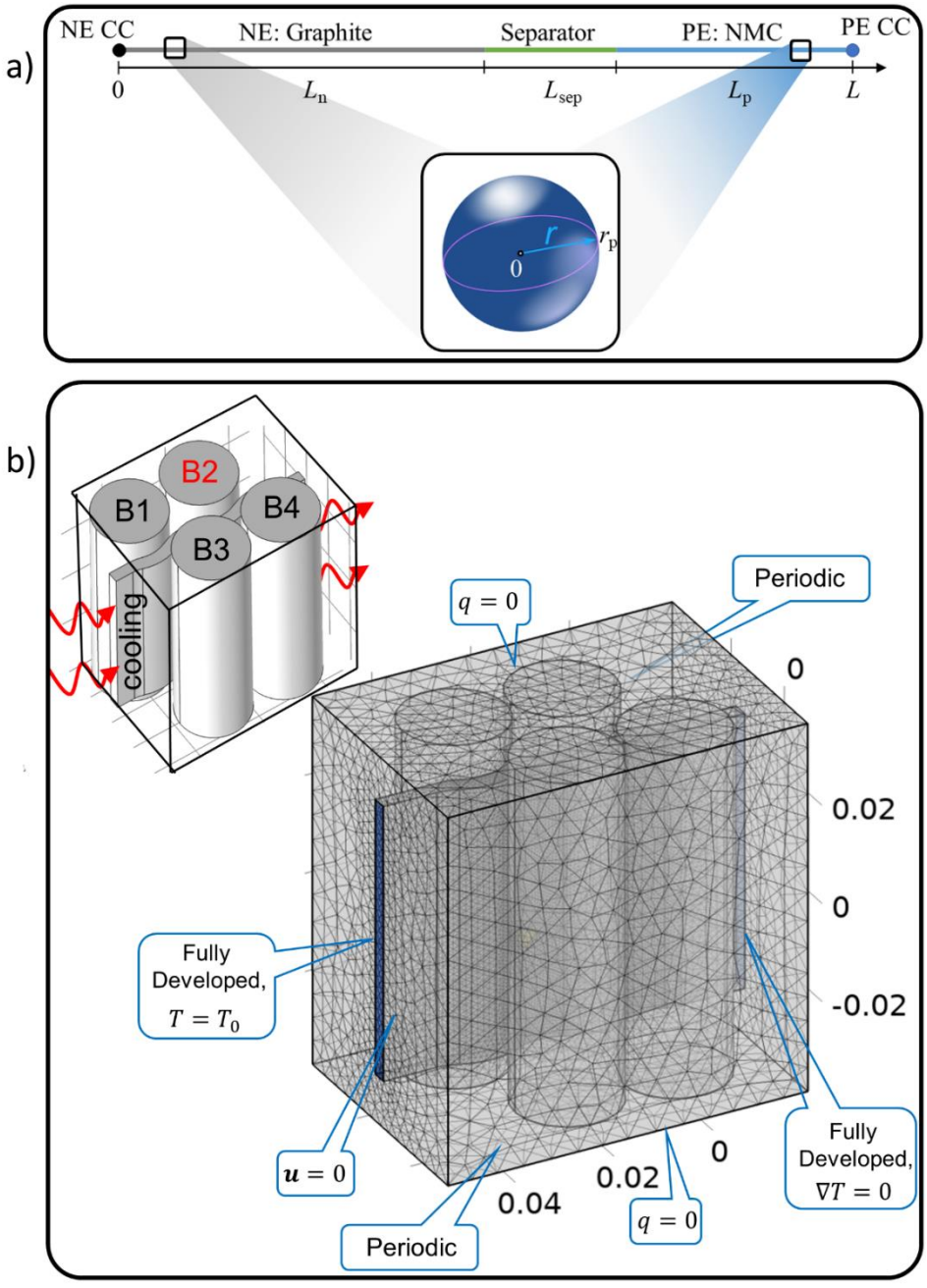

Fig. 16. Computational domain for the Multiphysics simulation showing a) the P2D model for the electrochemistry and b) the battery module representative unit with the cooling snake assembly and mesh illustration for the model showing all relevant boundary conditions for the 3D domain.

3.1.1.2 Model implementation

The mathematical model employed in this investigation integrates multi-scale and multi-domain methods and has been implemented using the COMSOL Multiphysics software [60]. The finite element model employs an unstructured mesh with quadratic elements and utilizes the backward Euler scheme for time discretization. The PARDISO solver from COMSOL 6.1 is used to solve the nonlinear equations system during both the initialization and transient stages. For the simulations presented in this chapter, a 3D model incorporating four cylindrical 2170 cells with NMC chemistry is selected. The cooling fluid comprises a 50% mixture of Ethylene Glycol and water. The negative electrodes consist of Graphite, while the positive electrode comprises NMC811. The electrolyte is composed of a 3:7 ratio of EC:EMC with a 1M $LiPF_6$ salt from the COMSOL material library. The model incorporates a user-defined condition, whereby the calculations are halted if the maximum temperature of the battery exceeds 500 K. This condition is crucial since exceeding this threshold can lead to a sudden temperature rise and potential explosion. Additionally, many parameters were used to perform the simulation obtained from prior literature. All those parameters used in the simulations shown in the results of this chapter are listed in Table 4.

Table 4. Model parameters for battery multiphysics model

Parameter	Value	Remarks
General		
System size	0.08x0.06x0.08 m	Assumed
Initial temperature	298 K	Assumed

Inlet flow velocity	0.1 m s^{-1}	Assumed
Cylindrical LIB related		
Form factor	2170	[89]
Dimensions		
Diameter	21 mm	[89]
Height	70 mm	
Thermal conductivity		
In-plane	30 W m^{-1} K^{-1}	[90]
Through-plane	1.29 W m^{-1} K^{-1}	
Negative electrode:		
Thickness	40 µm	Assumed
Particle radius	26.2 µm	Assumed
Solid phase volume fraction	0.58	[91–93]
Separator:		
Thickness	20 µm	[94–96]

Positive electrode:		
Thickness	35 µm	Assumed
Particle radius	10.7 µm	Assumed
Solid phase volume fraction	0.5	[94–96]
Charge transfer coefficient	0.5	
Electrolyte phase volume fraction	0.37	
Maximum voltage	4.2 V	[89]
Cut-off voltage	2.5 V	[89]
Capacity (typ.)	4800 mAh	[89]

3.1.2 ML methodology

The subsequent section is devoted to elucidating the proposed ML framework, which is divided into two distinct components. The initial part focuses on the preparation and preprocessing of the dataset, while the subsequent part delineates the implementation of the ML methodology. The ML methodology encompasses the spatio-temporal prediction of temperature, with the overarching objective of predicting TR in the battery system.

3.1.2.1 Dataset preparation and preprocessing for spatiotemporal ML study

Temperature forecasting constitutes a time-series prediction task, entailing the estimation of future temperature measurements based on historical temperature observations. Since temperature exhibits spatial variation along the thermocouple, I have established a coordinate network structured as a graph to represent the structured temperature time series as illustrated in Fig. 17. Consequently, any temperature observation at time step *t* is not independent but rather connected via pairwise connections in the graph. Thus, a data point at time step *t* can be conceptualized as a graph signal residing on an undirected graph.

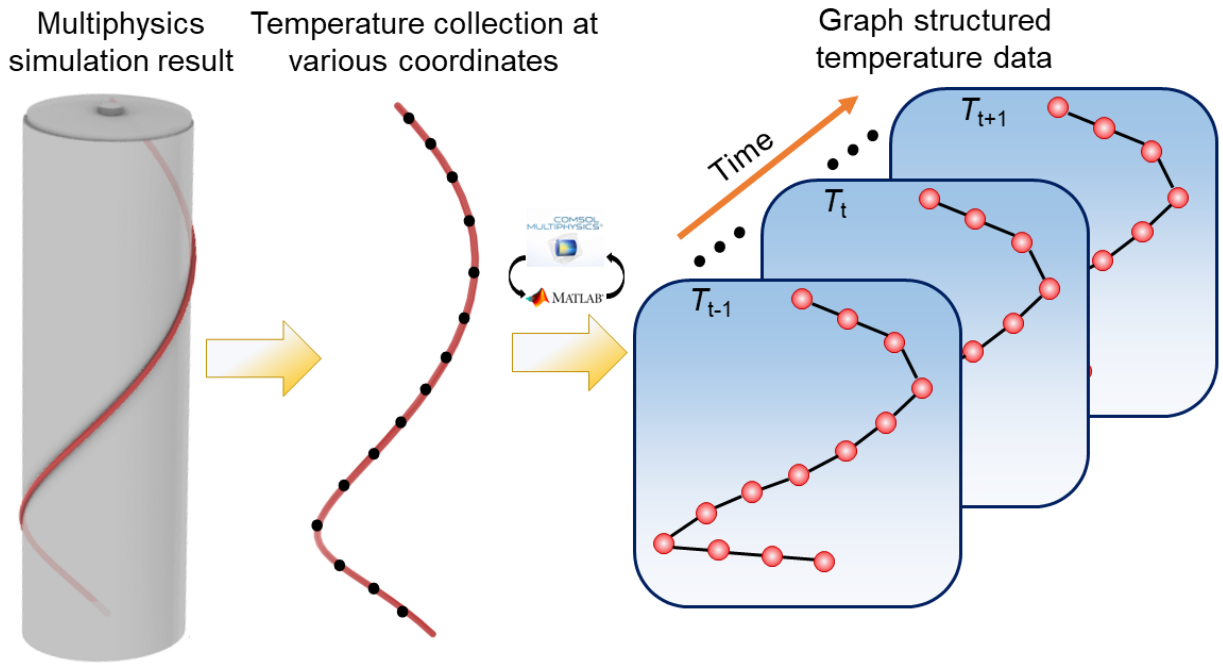

Fig. 17. Graph-structured temperature data. Each T_t indicates a frame of the current temperature graph for the thermocouple at time step t, which is recorded in a graph-structured data matrix. Figure is not to scale, just for visualization purposes only.

The extraction of relevant parameters for this problem encompasses the spatial coordinates along the thermocouple and the time-dependent temperature values. LiveLink for MATLAB was

employed to integrate COMSOL Multiphysics with MATLAB, facilitating the expansion of modeling capabilities through programming in the MATLAB environment. This bidirectional interface empowers the utilization of MATLAB as a scripting interface to configure and solve COMSOL Multiphysics models. By leveraging this functionality, temperature data along the spatial coordinates were extracted as CSV files for each time step of the battery's operation. However, these files cannot be directly employed for the ML study. Consequently, it is imperative to restructure the data into specific formats suitable for input into the ML study. This process, known as data preparation and preprocessing, constitutes a crucial step in any ML investigation. The aggregated data was modified and saved into two files. The first file contained the distances between the 120 spatial coordinates along the thermocouple, while the second file encompassed the temperature measurements collected at those points throughout the entire simulated battery operation. The first file contained the distance between the 120 spatial coordinates along the thermocouple, and the second file contained the temperature collected at those points for the entire time the battery was simulated. The first file is important for creating the adjacency matrix [97] required to create the graph network for spatial feature identification. An adjacency matrix is an $N \times N$ matrix filled with either 0 or 1, where N is the total number of nodes. Adjacency matrices are able to represent the existence of edges that connect the node pairs through the value in the matrices. In this work, the coordinates of the thermocouple are assumed to form a graph. The next step was to create the graph adjacency matrix from the distances calculated from the spatial coordinates. The estimation of the adjacency matrix was based on the work by Yu et al. [98] that assumes the presence of an edge between two nodes in the graph. Subsequently, I have generated the dataset necessary for tackling the forecasting problem. The challenge at hand revolves around envisioning forthcoming temperature measurements at various times. To accomplish this, I must

anticipate the temperature statistics during time intervals *which*+1, ..., *t*+*T*+*h*, based on the prior observations at *which*, *t*+2, ..., *t*+*T*. Consequently, our model receives *T* arrays comprising N elements, each as inputs for every given time t, while h arrays with N elements each serve as the desired outcomes. Here, N symbolizes the count of spatial points in consideration. Next, I split the temperature array into train/validation/test sets. The training dataset comprises 70% of the dataset, followed by 10% for validation and 20% for the test dataset. Finally, normalization was used for the resulting arrays.

3.1.2.2 Spatio-temporal prediction of temperature using graph neural network-long short-term memory

Current battery management systems provide real-time temperature readings; however, they lack the ability to predict future temperature trends. It is well-known that battery temperature can escalate rapidly due to internal degradation, potentially leading to TR. The occurrence of TR poses a significant safety risk as it can spread to neighboring cells and result in explosions. Therefore, the development of temperature forecasting methods becomes crucial. By utilizing the temperature history of batteries during operation, it becomes possible to predict future temperature trends, serving as a critical safety criterion for TR prognosis. In this context, data-driven approaches, particularly advanced ML techniques, offer great potential. However, traditional methods often fall short in capturing the nonlinear and complex nature of temperature profiles, thereby failing to meet the requirements of mid and long-term forecasting tasks. Additionally, these methods frequently overlook the spatial and temporal dependencies inherent in temperature data. To address these challenges, I have proposed a novel framework that combines a GNN with an LSTM network. This integrated GNN-LSTM network takes into account the intricate and variable temperature dependencies present in the historical data. By leveraging the power of GNNs

to handle spatial interdependencies and the temporal modeling capabilities of LSTMs, the proposed framework aims to forecast future temperature trends for battery modules accurately. The Convolutional layer in the GNN [99] enables learning and identification of a particular type of feature present at a specific spatial location within the input. Taking advantage of this capability, the GNN was employed to extract spatial features from the inputs using the coordinates of the thermocouple. Subsequently, the resulting output was utilized as the input for the LSTM in the subsequent step. LSTM [100], a type of Recurrent Neural Network (RNN), has been developed specifically for predicting future outputs by leveraging past inputs. LSTM has demonstrated its effectiveness in forecasting based on time-series data. Hence, LSTM was employed to forecast future temperature values by learning the relevant features embedded in the historical time-series data. Figure 18 shows the general network architecture of the proposed GNN-LSTM network. The architecture consists of a series of special layers to better capture the spatial and temporal dependencies of the data. The input layer accepts graph-structured time series data, where each node is associated with features in a series of time steps, and then the Graph Convolution (GC) layer applies graph convolution to gather information from neighboring nodes in order to facilitate the capture of spatial dependencies. The subsequent reshaping operation optimizes the output to match the LSTM levels. The LSTM layer formed with a specified number of units efficiently simulates the time dependence of the node embedding sequence. The outputs are reshaped again before feeding them into the flatten layer. Following the flatten layer, fully connected dense layers are used to transform the hidden state of the LSTM into predicted values for each node. This architecture showcases an intricate interplay of graph convolution and recurrent neural network components, illustrating a sophisticated approach for learning and forecasting on graph-structured

time series data. The workflow involves seamlessly passing information through these layers, collectively enabling the model to learn complex patterns and relationships within the graph.

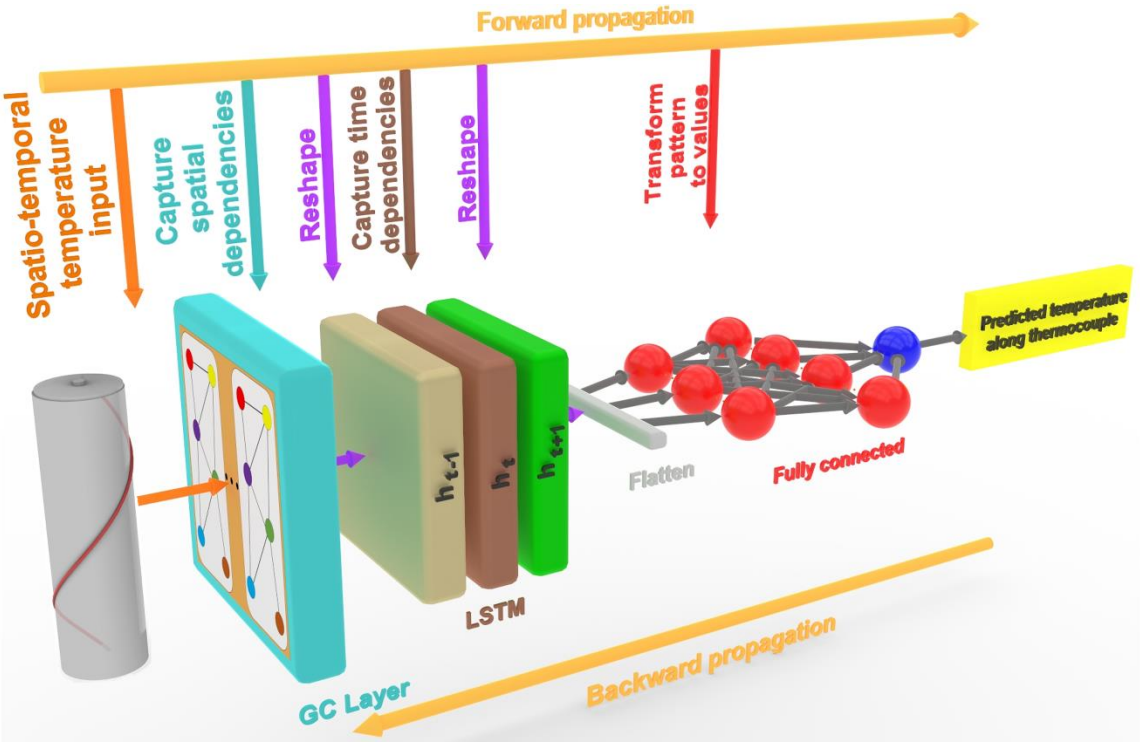

Fig. 18. Schematic of GNN-LSTM architecture. The input image is processed with a graph convolutional layer, and reshaping is used to introduce the information to the LSTM. Each memory cell is updated with weights from the previous cell. After this process, a flattened layer is used to transform the data into an arrangement to be read by a dense (fully connected) layer to give the final output.

3.2 Thermo-electrochemical modeling using constant charge/discharge cycles.

This section discusses the results pertaining to the multiphysics modeling under a constant charge/discharge load. TR in LIBs is a rapid and explosive event that poses challenges for real-time observation. During battery operation, various side reactions can be triggered [72],

potentially influencing the propagation of TR within the battery and leading to localized failure. Due to the complex nature of TR events and limited understanding, accurate modeling of TR remains challenging. In this modeling study, the selection of TR hotspots is performed randomly, considering scenarios with one or two hotspots. Figure 19 shows a general schematic on the location of the hotspots in battery B2 considered. Specifically, for Fig. 19a, the hotspot is located at coordinates (0.015, 0, 0). In Fig. 19b, the corresponding hotspot can be found at coordinates (0.015, 0, –0.0231). For Fig. 19c, there are two hotspots situated at (0.015, 0, 0.0231) and (0.015, 0, 0), and finally, Fig. 19d, which displays the two hotspots at (0.015, 0, 0.00581) and (0.015, 0, –0.0119). Each coordinate set represents the precise location of hotspots, underscoring the variability observed across the evaluated cases.

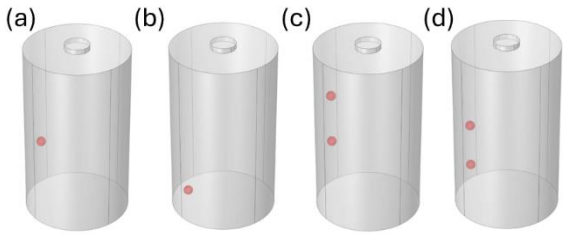

Fig. 19. Schematic showing the location of hotspots within the battery B2 undergoing degradation.

The presented results focus on constant charge/discharge load conditions. The voltage and temperature profiles for each battery are analyzed through multiphysics modeling. The influence of the SEI on battery temperature is discussed, followed by the visualization of high-temperature hotspots using temperature contours in the representative battery module unit. Before we dive into the TR modeling of cylindrical cells, I have first provided the validation of our developed electrochemical P2D model. The validation consists of the comparison between the discharge voltage characteristics obtained by the P2D model and the experimental data reported by Waldmann et al. [101]. For this purpose, the discharge curves were compared directly against the

experimental data at various discharge rates (cf. Fig. 20). The model's prediction is in good agreement with the experimental data during the initial discharge cycle, demonstrating the accuracy of the model.

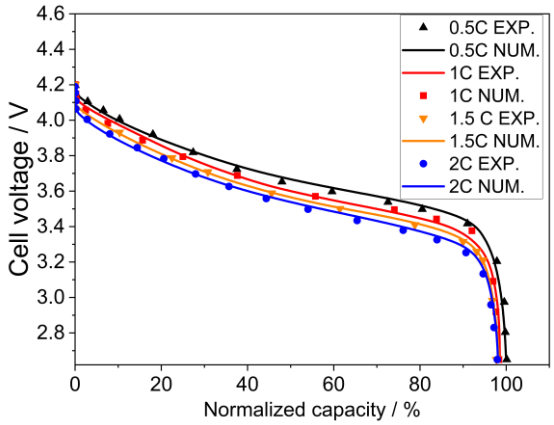

Fig. 20. Comparison of discharge characteristics for the P2D model (solid lines) and the experimental data (symbols) at different C rates.

Following this validation, the model is applied to study the impact of cell degradation on both the battery temperature and the capacity. To simulate this process, the CCCV charging and constant current discharging methods are utilized for all four batteries under investigation. Initially, the batteries are fully charged and subsequently discharged at a rate of 1C until reaching a cut-off voltage of 2.5 V. This discharge process is followed by CCCV charging of the batteries back to 4.2 V. Throughout the battery operation, the heat release is insufficient to trigger SEI decomposition, and the resulting temperature increase does not trigger TR. This observation is in good agreement with the fact that usually, at higher C rates, which indicate faster charging or discharging, more current flows through the battery. This increased current results in a higher rate of electrochemical reactions within the battery cells. Essentially, the faster the electrons are put in or out of the battery (a high C rate), the more resistance they encounter, and the more heat is

generated as a byproduct, increasing the risk of TR by initiating or exacerbating side reactions. Based on this observation, the cells are then operated at a higher rate of 2C. Based on this observation, the cells are then operated at a higher rate of 2C. Figure 21 shows the profile for charge and discharge curves for the four batteries with a single hotspot in battery B2 (cf. Fig. 21a), with a change in the maximum temperature for each battery (cf. Fig. 21b). In an optimal scenario, it is highly desirable for a battery to undergo a substantial number of charge-discharge cycles to facilitate a significant expansion of the SEI. It is widely assumed that there is negligible variation in the behavior exhibited from one cycle to another. Therefore, to effectively illustrate this concept, the growth rate of the SEI is accelerated by increasing the pre-exponential factor in the model. This assumption remains valid within the context of modeling, as it enables expedited observation of TR occurrences, thus facilitating more efficient analysis and understanding of battery behavior. Furthermore, this approach allows for the exploration of SEI expansion patterns and the potential effects on battery performance and safety under accelerated conditions, providing valuable insights for battery design and management strategies.

An important observation from Fig. 21a includes the characteristics of the voltage profile in battery B2. Since, B2 is subject to SEI degradation, it suffers from capacity fade and discharges faster compared to other batteries in the module. However, it should be mentioned that the BMS is engineered to safeguard each cell within a battery module by closely monitoring their individual voltages. It is essential to prevent any cell from discharging below its cutoff voltage, as this could lead to irreversible damage and compromise the pack's integrity. In practice, the BMS dynamically adjusts the current to individual cells based on their state. To mimic this behavior, I have used user defined condition that once the faulty battery B2 reaches its cutoff voltage sooner compared to other cells, the system specifically halts the discharging process for that cell to mitigate further

discharge. This selective intervention by the BMS exemplifies its crucial role in maintaining battery health and safety, ensuring that even as cells degrade at different rates, none are allowed to discharge beyond their safe limit. Similar observations can be made for the charging phase as well. Due to the lower capacity of battery B2, it reaches 4.2 V sooner than the other batteries, hence, the current supply is cut-off until the other batteries are fully charged. This trend in the rise of temperature due to the degradation of the battery has been well reported in prior literature. Prior literature [39,40] has shown the development of 1D and 3D models to estimate the temperature of evolution during TR. The researchers have documented a temperature shift that exhibits an exponential pattern reminiscent of the findings displayed in Figure 21b. It should be mentioned that the inclusion of hotpots would cause an uneven spread of heat within the battery, leading to an uneven formation of SEI. However, the P2D model, takes the SEI growth to be uniform for the negative electrode. Investigating the non-uniform generation of SEI necessitates the use of a three-dimensional particle model alongside a comprehensive battery model, which will be addressed in future research.

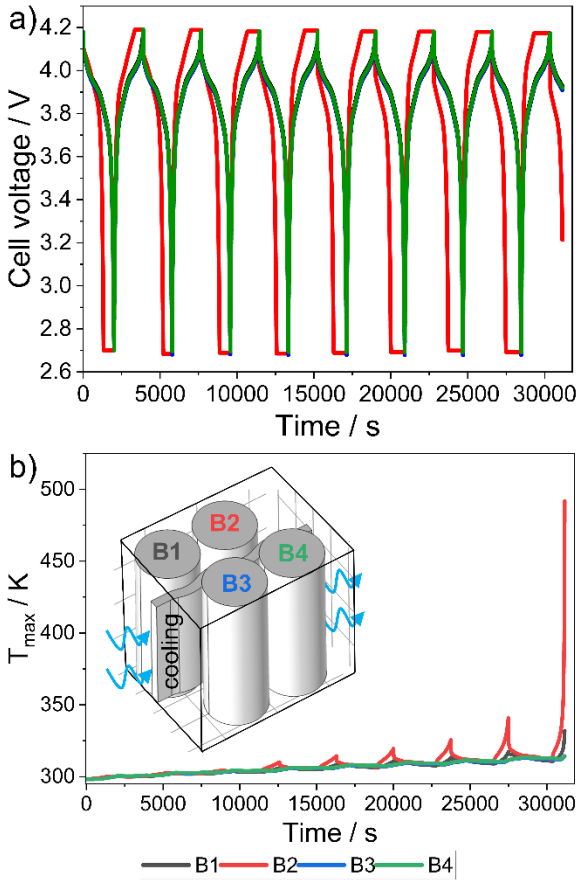

Fig. 21. Multiphysics modeling results illustrating the variation of general parameters relating to the electrochemical-thermal model with respect to time. (a) charge/discharge curves for one TR hotspot; (b) Maximum temperatures for the four Li-ion batteries.

Figure 22 illustrates the temporal evolution of the SEI layer thickness (depicted in blue) during the operational period of battery B2, along with the corresponding dynamics of the maximum battery temperature. Throughout the discharge process, exothermic phenomena prevail, resulting in the release of thermal energy, whereas during the charging phase, endothermic processes cause the battery to absorb a certain amount of heat. It should be noted that the system ceases operation once the predefined temperature limit of 500 K is reached, leading to an incomplete breakdown of the SEI layer, as evidenced in Figure 22. The disintegration of the SEI

layer generates heat, thereby elevating the battery temperature. The observed exponential rise in temperature can be attributed to the SEI decomposition reaction, which ultimately triggers TR within the battery. The model employed, incorporates a single Arrhenius function localized at the hotspot location, effectively representing the heat release arising from battery degradation. A similar exponential temperature increase trend has been reported by Belt and Sorensen [102] in their experimental investigation involving battery modules.

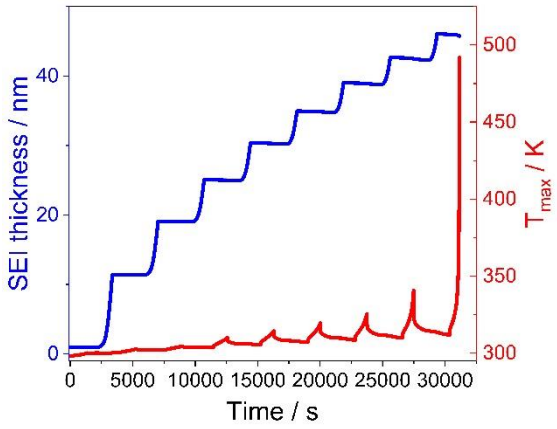

Fig. 22. Comparison of SEI thickness change (blue) during the battery operation for battery B2 with the corresponding change in the maximum temperature of the battery (red).

Precise modeling of TR presents significant challenges. The objective of constructing a TR model has been to derive temperature data from thermocouples attached to batteries, offering qualitative insights into TR initiation. The aim is to employ ML on simulation-derived data to predict TR. Here, artificial hotspots are introduced within batteries to trigger TR, with the number and locations of these hotspots being randomly distributed based on degradation mechanisms. Here, the number and locations of hotspots within battery B2 were varied to investigate the temporal evolution of cell temperature and its impact on neighboring cells. Figure 23 shows the temperature contours for the batteries at a constant 2C charge/discharge current. The heat release

from the SEI decomposition at the hotspot location for battery B2, causes the temperature of the entire battery to rise and eventually lead to the TR. Figures 23c & 23d show the temperature distribution for the batteries with battery B2 having two hotspots at different locations within the battery B2, and the location is given with respect to the height of the battery (h_{batt}). The exothermic reactions triggered by the decomposition of SEI release heat, leading to an increase in the overall battery temperature, which in turn triggers the occurrence of thermal TR.

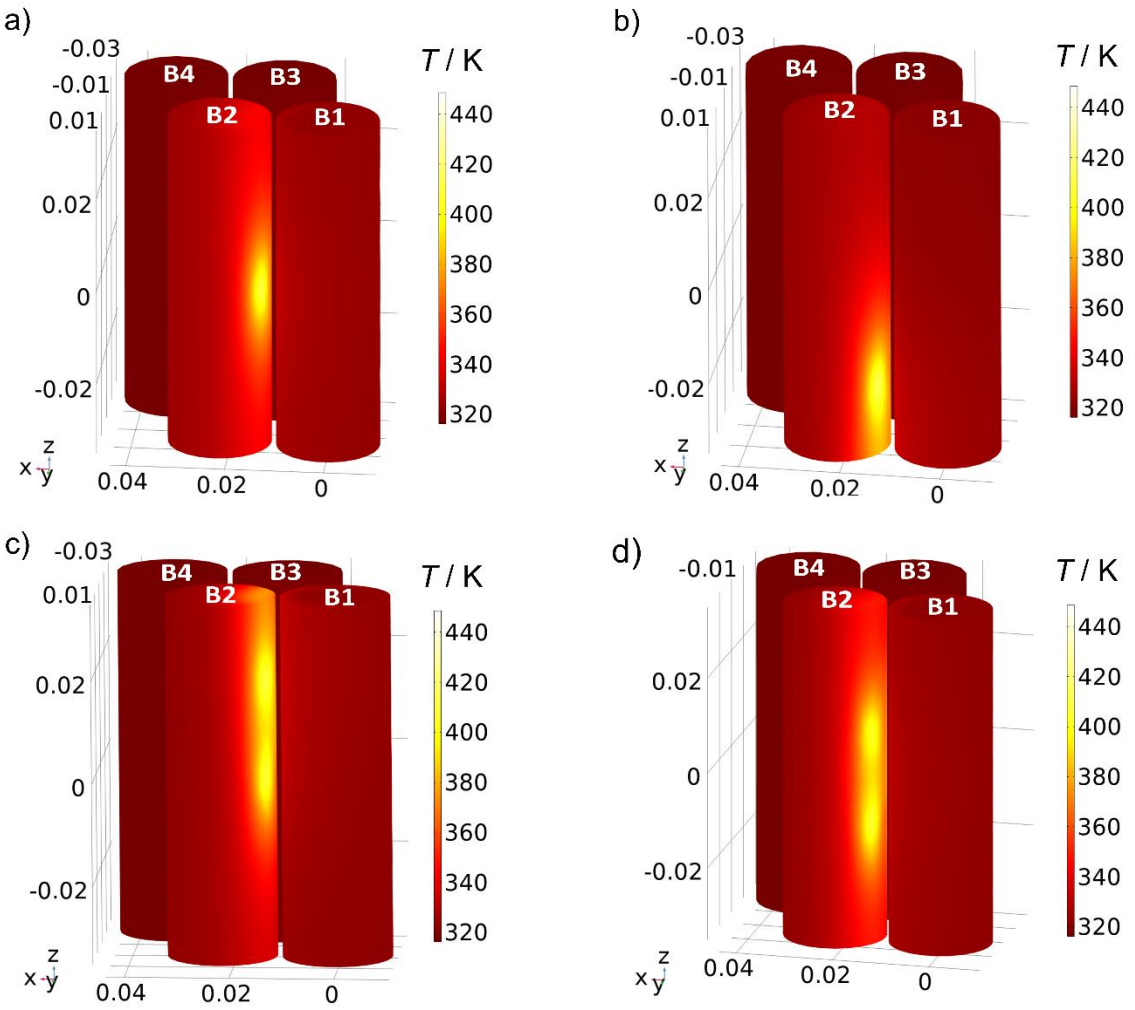

Fig. 23. Temperature contours for the surface of the batteries for single and two hotspots at 2C charge/discharge rate. a) Single hotspot at $0.5h_{batt}$ mm, b) single hotspot at $0.167h_{batt}$ mm from the bottom, c) two hotspots at $0.5h_{batt}$ mm and $0.83h_{batt}$ mm from the bottom, and d) two hotspots at $0.33h_{batt}$ mm and $0.583h_{batt}$ mm from the bottom. All hotspots are a distance of $\frac{3r_{batt}}{2}$ from the center of the battery in the radial direction.

3.3 Thermo-electrochemical modeling using driving cycle.

In this subsection, the focus shifts from the conventional constant charge-discharge cycle modeling to a more intricate and dynamic real-life scenario. Building upon the previous model, the transition to real driving cycle simulations marks a significant advancement in the understanding of TR in EVs. By incorporating real-world driving conditions and variations, this approach promises a more accurate representation of the complex interactions between temperature, electrochemical processes, and the real-world operating environments of LIB modules. The details on the driving cycle data utilized in this work are given in Fig. 24. Figure 24 shows all the important results pertaining to the driving cycle load. Figure 24a shows the typical FTP75 driving cycle obtained from EPA [49]. This driving cycle shows the variation of the speed of a car (mph) with time (s). The EPA driving cycle is provided for up to 1874 seconds. However, the batteries do not completely discharge in that short time frame. Hence, the EPA driving cycles are repeated after every 1874 seconds until the battery discharges to its lower cut-off voltage of 2.5 V. Figure 24b illustrates the corresponding current applied obtained from the driving cycle. The current profile is dictated by the acceleration, which depends exclusively on the profile of the applied driving cycle.

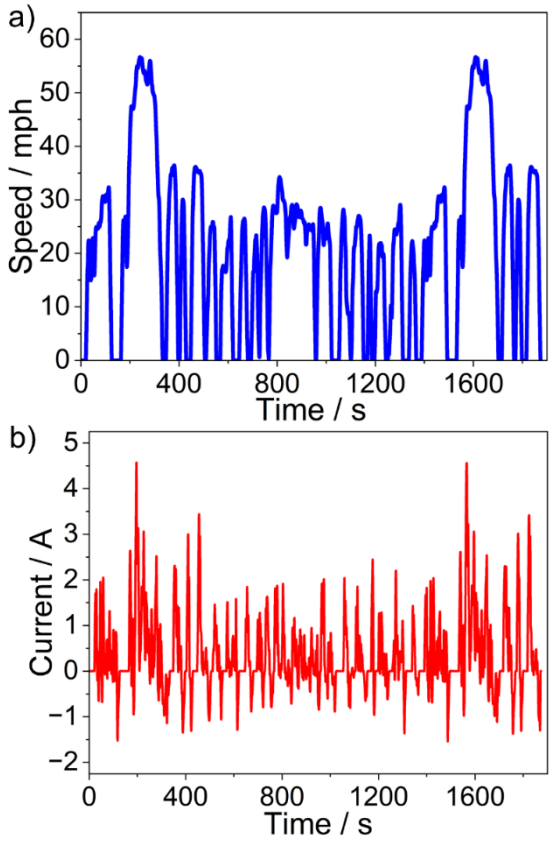

Fig. 24. Driving cycle characteristics. (a) Speed profile of the FTP75 driving cycle. (b) Discharging current for the duration of the FTP75 driving cycle

It has been assumed that the representative unit consisting of 4 batteries is fully charged initially, and then the driving cycle current is applied to it until the batteries reach the cut-off voltage. Upon completion of the discharge phase, the batteries are assumed to be charged at a constant current, mimicking the real-life scenario of a fully discharged EV plugged in for charge at a power outlet. Additionally, the governing equations and the corresponding boundary conditions pertaining to the batteries remain the same and have been well explained in the previous sections. Figure 25 shows the discharge/charge characteristics of the batteries in the representative unit, along with the effect of temperature due to SEI degradation. Figure 25a illustrates the

discharge/charge characteristics of the batteries subjected to driving cycle discharge and constant current charge. Similar to the previous model, SEI decomposition has been assumed to be the major degradation source in battery B2 only, and this is the battery that triggers TR when the temperature of 500 K is reached. Figure 25b shows the temperature evolution of the individual batteries of the representative unit with battery B2 undergoing SEI decomposition, which stems from internal defects already assumed to be present in the battery. This is a valid assumption, as any of the batteries in a battery module can have these local defects. Due to the presence of such local defects, they might become a source of degradation and consequently lead to high-temperature hotspots. These high-temperature hotspots result in increasing the temperature of the battery exponentially following an Arrhenius type of relation and lead to triggering a TR event.

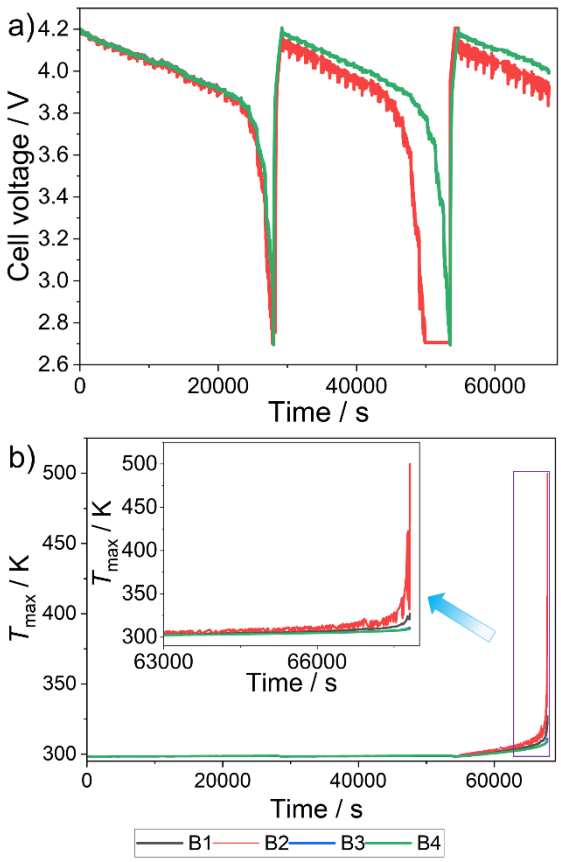

Fig. 25. Multiphysics modeling results for driving cycle-informed model illustrating the variation of general parameters relating to the electrochemical-thermal model with respect to time. (a) charge/discharge curves for one TR hotspot; (b) Maximum temperatures for the four Li-ion batteries.

Building upon the outcomes derived from the multiphysics simulation, the subsequent section will be dedicated to applying these findings within the context of the ML investigation. This will be succeeded by a comprehensive analysis of the results obtained.

3.4 Spatio-temporal ML results

The use of ML extensively expands the range of research possibilities for LIBs. Numerous ML techniques have demonstrated remarkable potential in examining the characteristics of materials used in LIBs, predicting the battery's SOC, and identifying instances of battery malfunctions [17,18,103]. ML has garnered considerable interest in recent times due to its effective implementations. A relatively novel strategy involves utilizing ML to anticipate TR occurrences in batteries. The existing body of literature contains scarce examples of employing data-oriented ML concepts for predicting such events. As far as I know, there has not been any research that utilizes a spatio-temporal ML technique to predict TR events using data collected from temperature sensors connected to a battery module, which is an unique aspect of our proposed framework. The information derived from the multiphysics modeling after proper data preprocessing is fed into the ML investigation to predict TR. This section is dedicated to the discussion of the results of the ML study. A learning curve, often called a plot of model's progress, illustrates how well the model learns over time. These curves are commonly employed in ML to train algorithms using iterative methods on a dataset. During training, the model undergoes training on a specific dataset and then undergoes evaluation on a separate validation dataset after each training iteration. The resulting performance measurements for both datasets across all iterations are graphed, resulting in the learning curve (cf. Figure 26). Learning curves aid in addressing issues such as underfitting or overfitting, as well as assessing the representativeness of the training and validation datasets. By examining the results presented in Fig. 26, it can be observed that all the networks exhibit satisfactory performance after 100 iterations, with the loss approaching approximately 0.02%. Similar patterns can be observed in the validation dataset.

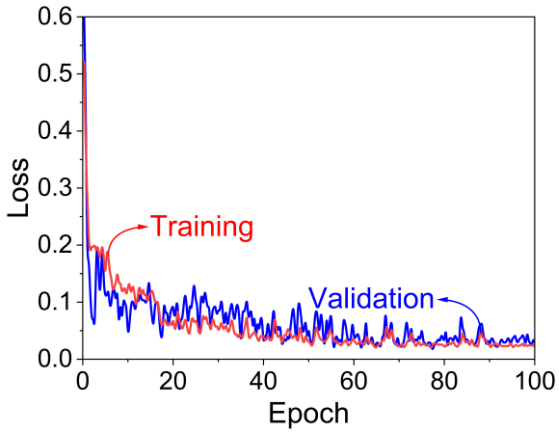

Fig. 26. Learning curve showing the loss with epoch on the training and the validation sets for the proposed GNN-LSTM network architecture.

Furthermore, an investigation was conducted to examine the impact of different training batch sizes on the overall model loss. Batch size [81] stands out as a critical tuning parameter in contemporary deep-learning systems. Preference is generally given to larger batch sizes, enabling the model to consider a greater amount of data during each training moment. However, larger batch sizes come with the drawbacks of increased computational memory consumption and prolonged training duration. In this particular analysis, the batch size varied to 32, 64, and 128 while maintaining the same number of training iterations. It is to be mentioned that these iterations are known as epochs in ML terminology. The comparison of loss between batch sizes of 64 and 128 yielded the most favorable outcomes for the proposed network, albeit the latter exhibited slightly higher accuracy at the expense of substantially greater training time and memory usage. Consequently, a batch size of 64 was selected as the optimal choice, and the outcomes were reported accordingly. Evaluation of the crucial statistical factors is vital in evaluating the model's effectiveness in predicting future outcomes. I have examined the efficiency of the suggested network by utilizing metrics such as the Mean Absolute Error (MAE) and Root Mean Squared

Error (RMSE), which have been considered to state the efficiency of the proposed network. Evaluation of the crucial statistical factors is vital in evaluating the model's effectiveness in predicting future outcomes. The concept of absolute deviation pertains to the size of the contrast between the projected outcome of an observation and the authentic value of that observation. Mean Absolute Error (MAE) calculates the mean value of absolute deviations for a set of projections and observations, serving as an assessment of the overall magnitude of discrepancies within the entire set. MAE is also recognized as the L1 loss function. Root Mean Square Error (RMSE) represents one of the primary performance evaluators for a regression model, quantifying the average variation between predicted values and actual values. It offers an approximation of the model's effectiveness in predicting the desired outcome. The MAE and RMSE of the proposed model are 0.072 and 0.187, respectively, on the test dataset. It is known that the test dataset is not known by the model during training, hence, such a lower value of these metrics indicates the efficiency of the proposed network. Additionally, the obtained values of the evaluation metrics indicate that this idea can also be well extended to data collected from experimental battery operation in EVs and could significantly help in predicting real-time TR detection in batteries. Figure 27 shows the ML results on the test dataset for the proposed network for the case with a single hotspot on battery B2 for three different orientations of thermocouples, namely of helix type (cf. Fig. 27a), helix+straight type (cf. Fig. 27b) and a U type (cf. Fig. 27c). The results are shown for the last 350 time steps where the TR is reached. Each time step relates to 1 second for the simulation, hence, the 350 time steps relate directly to the last 350 seconds for Fig. 21, representing the time from 30,806 seconds to 31,156 seconds when the simulation is stopped as TR happens. However, it should be noted that Fig. 21 shows the maximum internal temperature of the battery and Fig. 27 relates to the temperature obtained from the temperature sensors. The maximum internal temperature of the

battery essentially represents the temperature of the hotspots, which is higher than the local surface temperature. Figure 27 shows the ML forecasts for two different coordinates for each thermocouple. Upon analyzing the curves for ML forecasts (blue) and the true value (red), it can be well observed that the proposed model performs relatively well in predicting the time series temperature for various coordinates along the different thermocouples. It should be noted that for any ML study, the dataset should be normalized before training. Here, the normalization is being done using the z-score normalization and the temperature values on which the normalization was applied range from the initial temperature of 298K to the maximum internal temperature limit of 500K. Hence, the y-axis for the curves in Fig. 27 represents the normalized surface temperature. However, for ease of visualization and interpretation, the corresponding final temperature for the entire thermocouple is also provided with the legends given at the bottom of the figure.

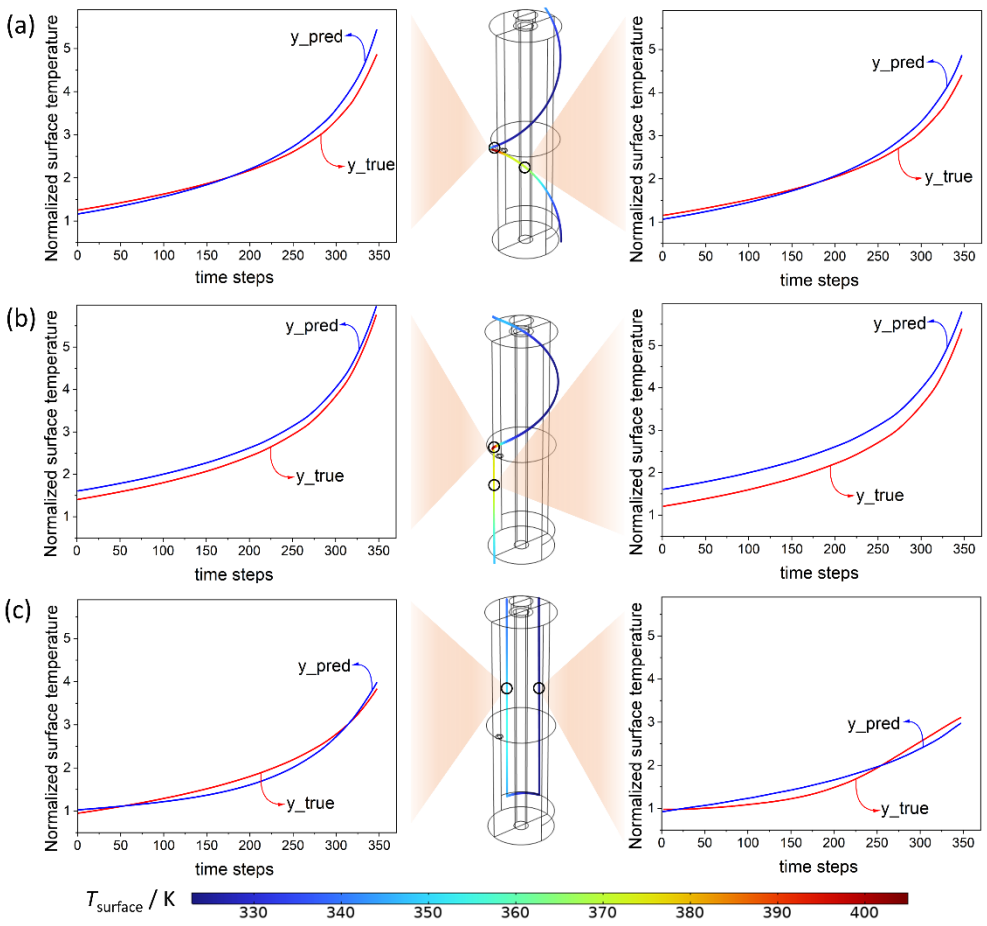

Fig. 27. ML results showing the temperature prediction of the GNN-LSTM model to forecast battery surface temperature series for the last 350 time steps along with the ground truth values with one hotspot on battery B2 on the test dataset of thermal sensors at 2 points along the sensor: a) helical type at (0.01427, 0.00711,–0.0022) (left) and (0.02452,0.01019, –0.01289) (Right), b) helix+straight type at (0.01271,–0.00531,0.00609) (left) and (0.01138,0, –0.01492) (right), c) U type at (0.02673,0.0095,–0.0003) (left) and (0.01732, 0.0095, –0.00031) (right). Due to constraints in ML methodology, surface temperatures are shown as normalized values. The legend at the bottom shows the corresponding values of the final temperature, as shown by the contour of the temperature sensor.

The proposed framework demonstrates remarkable effectiveness in accurately predicting temperature patterns over time, exhibiting minimal deviation from observed values. This statistical validation underscores the model's capability and reliability. The test dataset, consisting of completely unfamiliar samples to the model, ensures the model's ability to generalize to unseen data. The outstanding performance on this unknown dataset showcases the model's robustness and adaptability. The results strongly suggest the potential of employing various ML approaches to different configurations of thermocouples on battery cells, enabling precise prediction of thermal failures. This methodology can be further extended to real-time prediction of thermal failures in EVs, thus enhancing safety measures in EV applications.

3.5 Summary and conclusion

A novel framework has been developed to forecast the thermal response of cylindrical LIB module, integrating multiphysics modeling and ML techniques. The multiphysics model, implemented using COMSOL software, simulates the electrochemical-thermal characteristics of the cylindrical battery within the module under various conditions. The batteries are first subjected to constant current charge/discharge load cycles. The subsequent study involved the introduction of the driving cycle during the discharge phase to mimic the working of an EV in a real-life scenario. To capture real-world scenarios in practical battery module operation, thermal sensors are strategically positioned on the battery surface to extract battery surface temperature. The temperature data collected from the simulated thermocouples exhibits a complex nonlinear pattern that is dependent on both spatial and temporal variables. To address this complexity, an approach is proposed that combines a GNN capable of managing spatial interdependencies along the thermal sensors with an LSTM network that excels at handling temporal interdependencies.

Based upon the constant charge/discharge study, initially, the SEI layer grows rapidly during the charge cycles due to being limited by diffusion. Over time, as the layer becomes thicker, its resistance increases, which slows down the growth rate. Consequently, the system transitions from being diffusion-limited to being limited by kinetics. Additionally, the SEI formation led to the reduction of cyclable lithium, and significant capacity fade was observed. Due to this capacity fade, the battery B2 reached the cutoff voltage sooner and remained in the rest stage until all the other batteries were discharged to represent appropriate cell balancing. A similar trend was observed when the FTP 75 driving cycle was used. Moreover, the exponential rise in temperature caused by the exothermic heat release due to SEI decomposition in battery B2 was simulated, which has been explained by the Arrhenius equation. The ML results show outstanding performance in predicting the future temperature profiles along the coordinates of the temperature sensors with an MAE of 0.072 and an RMSE of 0.187 on the test dataset.

While this approach shows promise in enhancing the safety of EVs by predicting battery failures, there are challenges to its large-scale implementation. It is crucial to consider various degradation mechanisms and diverse cell designs to build a more comprehensive and reliable dataset than the current one. Moreover, we recognize the impact of diverse driving behaviors on battery temperature predictions. Our model's adaptability allows for retraining with varied driving data, enhancing its predictive capability for better safety outcomes. This flexibility ensures our approach remains effective across different operational scenarios, contributing to advancements in battery safety. Additionally, it should be noted that the versatile multiphysics modeling and ML framework reported in this chapter can be adapted to different configurations of LIBs, encompassing a range of geometric designs and diverse anode/cathode materials, extending beyond cylindrical cells.

CHAPTER 4. SUMMARY AND FUTURE WORK

This work represents a significant advancement in the field of LIBs, focusing on the prediction and prevention of TR in cylindrical LIBs. The study is methodically structured, beginning with an analysis of individual batteries and progressing to more complex battery module models. This comprehensive approach is vital for enhancing the safety of battery-operated devices, especially in high-stake applications like EVs and consumer electronics.

The initial phase of the research is dedicated to understanding the mechanisms of TR in a single cylindrical LIB and involves the prediction of such events. This investigation is crucial for identifying the fundamental causes and early warning signs of TR at the individual cell level. Utilizing COMSOL software, the study employs a multiphysics model to simulate the electrochemical and thermal behavior of cylindrical LIBs under various conditions. This model is a cornerstone in understanding the internal dynamics of these batteries, particularly how they respond to different environmental and operational stressors. The study then incorporates deep learning techniques for predicting TR, with a significant focus on real-time prediction using CNNs. CNNs are employed to process thermal images of the battery, identifying patterns and anomalies that could lead to TR. Additionally, the YOLO object detection algorithm is applied to these images to detect high-temperature hotspots, which are crucial for pinpointing potential TR sites within the battery. A key aspect of this phase of the study is the emphasis on using the maximum temperature as a primary benchmark for TR classification, due to its direct correlation with critical thermal conditions within the battery.

Building upon the insights gained from the single battery study, the research extends to battery module modeling. This transition is critical for addressing the complexities associated with TR in battery modules, which involve multiple interconnected cells and present a more intricate

scenario compared to individual batteries. The study explores the spatio-temporal temperature dynamics within these modules, recognizing the importance of understanding how heat is distributed and evolves over time among interconnected cells. To effectively model these dynamics, the research introduces a novel framework that combines GNNs and LSTM networks. GNNs adeptly manage the spatial relationships among thermal sensors placed on the battery module, while LSTMs process the temporal data patterns, providing a comprehensive understanding of the thermal behavior in battery modules. This innovative approach significantly enhances the ability to predict TR events in more complex battery configurations.

Throughout the thesis, several challenges and practical considerations are acknowledged. One of the main challenges is acquiring accurate thermal images, which is crucial for the DL models to function effectively. The study also addresses the high initial costs associated with setting up such a predictive framework and the substantial data storage solutions required for handling large volumes of thermal imaging data. Moreover, the research highlights the necessity of considering a broader range of cell designs and degradation mechanisms to ensure the robustness and broader applicability of the predictive models.

In terms of future work, the thesis suggests several avenues for exploration and application. It advocates for the expansion of the dataset to include a wider variety of cell designs and degradation types, which would enhance the model's reliability and applicability. Continuous refinement of the ML/DL models is emphasized for achieving higher accuracy and efficiency, particularly for real-time applications. The study also suggests extending these methodologies to other types of batteries, broadening the scope and impact of this research in the field of battery safety. Addressing the challenges of real-world implementation, including cost-effectiveness and data management, is highlighted as crucial for the practical application of these frameworks.

Lastly, the integration of these predictive models with existing battery management systems could offer a holistic approach to monitoring and maintaining battery health and safety, providing a comprehensive solution for a wide range of battery-powered devices and systems.

In conclusion, this work makes a substantial contribution to the field of battery safety and management. The transition from analyzing single batteries to modeling battery modules reflects a significant advancement, offering groundbreaking methodologies for predicting and preventing TR in cylindrical LIBs. The implications of this research are far-reaching, with potential applications in enhancing the safety and reliability of a multitude of battery-powered devices and systems.

APPENDIX

Table 5. List of abbreviations

Abbreviations	Full forms
AI	Artificial intelligence
ARIMA	Autoregressive integrated moving average
BMS	Battery management system
CCCV	Constant current constant voltage
CNN	Convolutional neural networks
DL	Deep learning
EC	Ethylene carbonate
EMC	Ethyl methyl carbonate
EPA	Environmental Protection Agency
EV	Electric vehicles
FEM	Finite element method
FN	False negative
FP	False positive
FTP	Federal test procedure
GC	Graph Convolution
GNN	Graph neural network
GPR	Gaussian process regression
HGR	Heat generation rate
KNN	K nearest neighbor
LCO	Lithium cobalt oxide
LEDC	Lithium ethylene dicarbonate
LIB	Lithium ion battery
LSTM	Long short term memory
MAE	Mean absolute error
ML	Machine learning
NAS	Neural architecture search
NMC	Nickel Manganese Cobalt
NN	Neural network
PHM	Prognostic health management
PHS	Pumped hydroelectric storage
RGB	Red green blue
RMSE	Root mean squared error
RNN	Recurrent neural network
RUL	Remaining useful life
RVM	Relevance vector machine
SEI	Solid electrolyte interface
SGD	Stochastic gradient descent
SOC	State of charge
SOH	State of health
SVM	Support vector machine
TEM	Transmission electron microscopy

TES	Thermal energy storage
TN	True negative
TP	True positive
TPR	True positive rate
TR	Thermal runaway
VGG	Visual geometry group
YOLO	You only look once

REFERENCES

[1] https://www.energy.gov/eere/water/pumped-storage-hydropower, (n.d.).

[2] https://www.iea.org/energy-system/electricity/grid-scale-storage, (n.d.).

[3] https://www.irena.org/Energy-Transition/Technology/Energy-Storage, (n.d.).

[4] Y. Yang, E.G. Okonkwo, G. Huang, S. Xu, W. Sun, Y. He, On the sustainability of lithium ion battery industry – A review and perspective, Energy Storage Mater. 36 (2021) 186–212. https://doi.org/10.1016/j.ensm.2020.12.019.

[5] N. Nitta, F. Wu, J.T. Lee, G. Yushin, Li-ion battery materials: Present and future, Mater. Today. 18 (2015) 252–264. https://doi.org/10.1016/j.mattod.2014.10.040.

[6] F. Schipper, D. Aurbach, A brief review: Past, present and future of lithium ion batteries, Russ. J. Electrochem. 52 (2016) 1095–1121. https://doi.org/10.1134/S1023193516120120.

[7] H. Li, C. Liu, A. Saini, Y. Wang, H. Jiang, T. Yang, L. Chen, C. Pan, H. Shen, Coupling multi-physics simulation and response surface methodology for the thermal optimization of ternary prismatic lithium-ion battery, J. Power Sources. 438 (2019) 226974. https://doi.org/10.1016/j.jpowsour.2019.226974.

[8] E. Hosseinzadeh, J. Marco, P. Jennings, Electrochemical-Thermal Modelling and Optimisation of Lithium-Ion Battery Design Parameters Using Analysis of Variance, Energies. 10 (2017) 1278. https://doi.org/10.3390/en10091278.

[9] W. Zhang, Z. Liang, X. Yin, G. Ling, Avoiding thermal runaway propagation of lithium-ion battery modules by using hybrid phase change material and liquid cooling, Appl. Therm. Eng. 184 (2021) 116380. https://doi.org/10.1016/j.applthermaleng.2020.116380.

[10] J. Xu, C. Lan, Y. Qiao, Y. Ma, Prevent thermal runaway of lithium-ion batteries with minichannel cooling, Appl. Therm. Eng. 110 (2017) 883–890. https://doi.org/10.1016/j.applthermaleng.2016.08.151.

[11] J. Newman, W. Tiedemann, POROUS-ELECTRODE THEORY WITH BATTERY APPLICATIONS, (1974). https://cloudfront.escholarship.org/dist/prd/content/qt9vd6z2g7/qt9vd6z2g7.pdf.

[12] H. Gu, T. V. Nguyen, R.E. White, A Mathematical Model of a Lead-Acid Cell: Discharge, Rest, and Charge, J. Electrochem. Soc. 134 (1987) 2953–2960. https://doi.org/10.1149/1.2100322.

[13] A. Melcher, C. Ziebert, M. Rohde, H. Seifert, Modeling and Simulation of the Thermal Runaway Behavior of Cylindrical Li-Ion Cells—Computing of Critical Parameters, Energies. 9 (2016) 292. https://doi.org/10.3390/en9040292.

[14] Z. Wang, W. Fan, P. Liu, Simulation of Temperature Field of Lithium Battery Pack Based on Computational Fluid Dynamics, Energy Procedia. 105 (2017) 3339–3344. https://doi.org/10.1016/j.egypro.2017.03.764.

[15] R.D. Jilte, R. Kumar, Numerical investigation on cooling performance of Li-ion battery thermal management system at high galvanostatic discharge, Eng. Sci. Technol. an Int. J. 21 (2018) 957–969. https://doi.org/10.1016/j.jestch.2018.07.015.

[16] T. Albrecht, S. Horswell, L.K. Allerston, N. V. Rees, P. Rodriguez, Electrochemical processes at the nanoscale, Curr. Opin. Electrochem. 7 (2018) 138–145. https://doi.org/10.1016/j.coelec.2017.11.016.

[17] D.P. Finegan, S.J. Cooper, Battery Safety: Data-Driven Prediction of Failure, Joule. 3 (2019) 2599–2601. https://doi.org/10.1016/j.joule.2019.10.013.

[18] M. Ragone, V. Yurkiv, A. Ramasubramanian, B. Kashir, F. Mashayek, Data driven estimation of electric vehicle battery state-of-charge informed by automotive simulations and multi-physics modeling, J. Power Sources. 483 (2021) 229108. https://doi.org/10.1016/j.jpowsour.2020.229108.

[19] S. Song, C. Fei, H. Xia, Lithium-Ion Battery SOH Estimation Based on XGBoost Algorithm with Accuracy Correction, Energies. 13 (2020) 812. https://doi.org/10.3390/en13040812.

[20] H. Rauf, M. Khalid, N. Arshad, Machine learning in state of health and remaining useful life estimation: Theoretical and technological development in battery degradation modelling, Renew. Sustain. Energy Rev. 156 (2022) 111903. https://doi.org/10.1016/j.rser.2021.111903.

[21] E. Cripps, M. Pecht, A Bayesian nonlinear random effects model for identification of defective batteries from lot samples, J. Power Sources. 342 (2017) 342–350. https://doi.org/10.1016/j.jpowsour.2016.12.067.

[22] J.C. Álvarez Antón, P.J. García Nieto, F.J. de Cos Juez, F. Sánchez Lasheras, M. González Vega, M.N. Roqueñí Gutiérrez, Battery state-of-charge estimator using the SVM technique, Appl. Math. Model. 37 (2013) 6244–6253. https://doi.org/10.1016/j.apm.2013.01.024.

[23] R.R. Richardson, M.A. Osborne, D.A. Howey, Gaussian process regression for forecasting battery state of health, J. Power Sources. 357 (2017) 209–219. https://doi.org/10.1016/j.jpowsour.2017.05.004.

[24] R.R. Richardson, M.A. Osborne, D.A. Howey, Battery health prediction under generalized conditions using a Gaussian process transition model, J. Energy Storage. 23 (2019) 320–

328. https://doi.org/10.1016/j.est.2019.03.022.

[25] A. Widodo, M.C. Shim, W. Caesarendra, B.S. Yang, Intelligent prognostics for battery health monitoring based on sample entropy, Expert Syst. Appl. 38 (2011) 11763–11769. https://doi.org/10.1016/j.eswa.2011.03.063.

[26] A. Vaswani, N. Shazeer, N. Parmar, J. Uszkoreit, L. Jones, A.N. Gomez, Ł. Kaiser, I. Polosukhin, Attention is All you Need, in: I. Guyon, U. Von Luxburg, S. Bengio, H. Wallach, R. Fergus, S. Vishwanathan, R. Garnett (Eds.), Adv. Neural Inf. Process. Syst., Curran Associates, Inc., 2017. https://proceedings.neurips.cc/paper_files/paper/2017/file/3f5ee243547dee91fbd053c1c4a845aa-Paper.pdf.

[27] S. Ahmed, I.E. Nielsen, A. Tripathi, S. Siddiqui, R.P. Ramachandran, G. Rasool, Transformers in Time-Series Analysis: A Tutorial, Circuits, Syst. Signal Process. 42 (2023) 7433–7466. https://doi.org/10.1007/s00034-023-02454-8.

[28] D. Shi, J. Zhao, Z. Wang, H. Zhao, J. Wang, Y. Lian, A.F. Burke, Spatial-Temporal Self-Attention Transformer Networks for Battery State of Charge Estimation, Electronics. 12 (2023) 2598. https://doi.org/10.3390/electronics12122598.

[29] H. Shen, X. Zhou, Z. Wang, J. Wang, State of charge estimation for lithium-ion battery using Transformer with immersion and invariance adaptive observer, J. Energy Storage. 45 (2022) 103768. https://doi.org/10.1016/j.est.2021.103768.

[30] G.E. Box, G.M. Jenkins, G.C. Reinsal, Time series analysis: forecasting and control, 5th editio, John Wiley & Sons, n.d.

[31] J. Liu, A. Saxena, K. Goebel, B. Saha, W. Wang, An adaptive recurrent neural network for remaining useful life prediction of lithium-ion batteries, Annu. Conf. Progn. Heal.

Manag. Soc. PHM 2010. (2010) 0–9.

[32] S. Lee, S. Han, K.H. Han, Y. Kim, S. Agarwal, K.S. Hariharan, B. Oh, J. Yoon, Diagnosing various failures of lithium-ion batteries using artificial neural network enhanced by likelihood mapping, J. Energy Storage. 40 (2021) 102768. https://doi.org/10.1016/j.est.2021.102768.

[33] L. Jiang, Z. Deng, X. Tang, L. Hu, X. Lin, X. Hu, Data-driven fault diagnosis and thermal runaway warning for battery packs using real-world vehicle data, Energy. 234 (2021) 121266. https://doi.org/10.1016/j.energy.2021.121266.

[34] S. Ding, C. Dong, T. Zhao, L. Koh, X. Bai, J. Luo, A Meta-learning Based Multimodal Neural Network for Multistep Ahead Battery Thermal Runaway Forecasting, IEEE Trans. Ind. Informatics. 17 (2021) 4503–4511. https://doi.org/10.1109/TII.2020.3015555.

[35] R. Yang, R. Xiong, W. Shen, X. Lin, Extreme Learning Machine-Based Thermal Model for Lithium-Ion Batteries of Electric Vehicles under External Short Circuit, Engineering. 7 (2021) 395–405. https://doi.org/10.1016/j.eng.2020.08.015.

[36] O. Ojo, H. Lang, Y. Kim, X. Hu, B. Mu, X. Lin, A Neural Network Based Method for Thermal Fault Detection in Lithium-Ion Batteries, IEEE Trans. Ind. Electron. 68 (2021) 4068–4078. https://doi.org/10.1109/TIE.2020.2984980.

[37] D. Li, P. Liu, Z. Zhang, L. Zhang, J. Deng, Z. Wang, D.G. Dorrell, W. Li, D.U. Sauer, Battery Thermal Runaway Fault Prognosis in Electric Vehicles Based on Abnormal Heat Generation and Deep Learning Algorithms, IEEE Trans. Power Electron. 37 (2022) 8513–8525. https://doi.org/10.1109/TPEL.2022.3150026.

[38] S. Abada, G. Marlair, A. Lecocq, M. Petit, V. Sauvant-Moynot, F. Huet, Safety focused modeling of lithium-ion batteries: A review, J. Power Sources. 306 (2016) 178–192.

https://doi.org/10.1016/j.jpowsour.2015.11.100.

[39] T.D. Hatchard, D.D. MacNeil, A. Basu, J.R. Dahn, Thermal Model of Cylindrical and Prismatic Lithium-Ion Cells, J. Electrochem. Soc. 148 (2001) A755. https://doi.org/10.1149/1.1377592.

[40] G.H. Kim, A. Pesaran, R. Spotnitz, A three-dimensional thermal abuse model for lithium-ion cells, J. Power Sources. 170 (2007) 476–489. https://doi.org/10.1016/j.jpowsour.2007.04.018.

[41] H. Maleki, J.N. Howard, Internal short circuit in Li-ion cells, J. Power Sources. 191 (2009) 568–574. https://doi.org/10.1016/j.jpowsour.2009.02.070.

[42] M.N. Richard, J.R. Dahn, Accelerating Rate Calorimetry Study on the Thermal Stability of Lithium Intercalated Graphite in Electrolyte. II. Modeling the Results and Predicting Differential Scanning Calorimeter Curves, J. Electrochem. Soc. 146 (1999) 2078–2084. https://doi.org/10.1149/1.1391894.

[43] B.R. Das Goswami, M. Mastrogiorgio, M. Ragone, F. Mashayek, V. Yurkiv, Predicting Thermal Failures Using an Advanced Data-Driven Modeling Framework in a Cylindrical Li-Ion Battery Pack, ECS Meet. Abstr. MA2022-02 (2022) 230–230. https://doi.org/10.1149/MA2022-023230mtgabs.

[44] B.R. Das Goswami, M. Mastrogiorgio, M. Ragone, F. Mashayek, V. Yurkiv, A Combined Multi-Physics Modelling and Machine Learning to Predict Electro-Thermal Failures of Cylindrical Li-Ion Batteries, ECS Meet. Abstr. MA2022-01 (2022) 190–190. https://doi.org/10.1149/MA2022-012190mtgabs.

[45] M. Mastrogiorgio, B.R. Das Goswami, M. Ragone, F. Mashayek, V. Yurkiv, Advanced Data-Driven Modeling Framework for Predicting Thermal Failures in Li-Ion Pouch

Batteries, ECS Meet. Abstr. MA2022-01 (2022) 434–434. https://doi.org/10.1149/MA2022-012434mtgabs.

[46] T. Yamanaka, Y. Takagishi, T. Yamaue, A Framework for Optimal Safety Li-ion Batteries Design using Physics-Based Models and Machine Learning Approaches, J. Electrochem. Soc. 167 (2020) 100516. https://doi.org/10.1149/1945-7111/ab975c.

[47] A. Naha, A. Khandelwal, S. Agarwal, P. Tagade, K.S. Hariharan, A. Kaushik, A. Yadu, S.M. Kolake, S. Han, B. Oh, Internal short circuit detection in Li-ion batteries using supervised machine learning, Sci. Rep. 10 (2020) 1–10. https://doi.org/10.1038/s41598-020-58021-7.

[48] J. Redmon, S. Divvala, R. Girshick, A. Farhadi, You only look once: Unified, real-time object detection, Proc. IEEE Comput. Soc. Conf. Comput. Vis. Pattern Recognit. 2016-Decem (2016) 779–788. https://doi.org/10.1109/CVPR.2016.91.

[49] M. Doyle, T.F. Fuller, J. Newman, Modeling of Galvanostatic Charge and Discharge of the Lithium/Polymer/Insertion Cell, J. Electrochem. Soc. 140 (1993) 1526–1533. https://doi.org/10.1149/1.2221597.

[50] J. Newman, W. Tiedemann, Potential and Current Distribution in Electrochemical Cells: Interpretation of the Half-Cell Voltage Measurements as a Function of Reference-Electrode Location, J. Electrochem. Soc. 140 (1993) 1961–1968. https://doi.org/10.1149/1.2220746.

[51] Y. Chen, J.W. Evans, Three-Dimensional Thermal Modeling of Lithium-Polymer Batteries under Galvanostatic Discharge and Dynamic Power Profile, J. Electrochem. Soc. 141 (1994) 2947–2955. https://doi.org/10.1149/1.2059263.

[52] M. Doyle, J. Newman, A.S. Gozdz, C.N. Schmutz, J. Tarascon, Comparison of Modeling

Predictions with Experimental Data from Plastic Lithium Ion Cells, J. Electrochem. Soc. 143 (1996) 1890–1903. https://doi.org/10.1149/1.1836921.

[53] H. Ekström, G. Lindbergh, A Model for Predicting Capacity Fade due to SEI Formation in a Commercial Graphite/LiFePO 4 Cell , J. Electrochem. Soc. 162 (2015) A1003–A1007. https://doi.org/10.1149/2.0641506jes.

[54] K.S. Hariharan, P. Tagade, S. Ramachandran, Mathematical Modeling of Lithium Batteries, Springer International Publishing, Cham, 2018. https://doi.org/10.1007/978-3-319-03527-7.

[55] T. Katrašnik, I. Mele, K. Zelič, Multi-scale modelling of Lithium-ion batteries: From transport phenomena to the outbreak of thermal runaway, Energy Convers. Manag. 236 (2021) 114036. https://doi.org/10.1016/j.enconman.2021.114036.

[56] B.S. Parimalam, A.D. MacIntosh, R. Kadam, B.L. Lucht, Decomposition Reactions of Anode Solid Electrolyte Interphase (SEI) Components with LiPF6, J. Phys. Chem. C. 121 (2017) 22733–22738. https://doi.org/10.1021/acs.jpcc.7b08433.

[57] G. Qian, F. Monaco, D. Meng, S.-J. Lee, G. Zan, J. Li, D. Karpov, S. Gul, D. Vine, B. Stripe, J. Zhang, J.-S. Lee, Z.-F. Ma, W. Yun, P. Pianetta, X. Yu, L. Li, P. Cloeten, Y. Liu, The role of structural defects in commercial lithium-ion batteries, Cell Reports Phys. Sci. 2 (2021) 100554. https://doi.org/10.1016/j.xcrp.2021.100554.

[58] M.R. Gerhardt, A.A. Wong, M.J. Aziz, The Effect of Interdigitated Channel and Land Dimensions on Flow Cell Performance, J. Electrochem. Soc. 165 (2018) A2625–A2643. https://doi.org/10.1149/2.0471811jes.

[59] W. Liao, Statistical properties of solutions to the Navier-Stokes equation in the limit of vanishing viscosity, J. Phys. A. Math. Gen. 22 (1989) L737–L741.

https://doi.org/10.1088/0305-4470/22/15/004.

[60] Comsol Multiphysics® v. 5.6, COMSOL AB, Stock. Sweden.,(n.D.). (2021). www.comsol.com.

[61] S.M. Abd Elrahman, A. Abraham, A Review of Class Imbalance Problem, J. Netw. Innov. Comput. 1 (2013) 332–340. www.mirlabs.net/jnic/index.html.

[62] D.A.V. Dyk, X.L. Meng, The art of data augmentation, J. Comput. Graph. Stat. 10 (2001) 1–50. https://doi.org/10.1198/10618600152418584.

[63] S.G.K. Patro, K.K. sahu, Normalization: A Preprocessing Stage, Iarjset. 2 (2015) 20–22. https://doi.org/10.17148/iarjset.2015.2305.

[64] F. Herrera, F. Charte, A.J. Rivera, M.J. del Jesus, Multilabel Classification, in: Multilabel Classif., Springer International Publishing, Cham, 2016: pp. 17–31. https://doi.org/10.1007/978-3-319-41111-8_2.

[65] O. Fagbohungbe, L. Qian, Benchmarking Inference Performance of Deep Learning Models on Analog Devices, Proc. Int. Jt. Conf. Neural Networks. 2021-July (2021) 1–9. https://doi.org/10.1109/IJCNN52387.2021.9534143.

[66] M. Tan, Q. V. Le, EfficientNet: Rethinking Model Scaling for Convolutional Neural Networks, Int. Conf. Mach. Learn. (2019). https://doi.org/https://doi.org/10.48550/arXiv.1905.11946.

[67] K. Lin, Y. Zhao, X. Gao, M. Zhang, C. Zhao, L. Peng, Q. Zhang, T. Zhou, Applying a deep residual network coupling with transfer learning for recyclable waste sorting, Environ. Sci. Pollut. Res. 29 (2022) 91081–91095. https://doi.org/10.1007/s11356-022-22167-w.

[68] K. Simonyan, A. Zisserman, Very deep convolutional networks for large-scale image

recognition, 3rd Int. Conf. Learn. Represent. ICLR 2015 - Conf. Track Proc. (2015) 1–14.

[69] K. He, X. Zhang, S. Ren, J. Sun, Deep residual learning for image recognition, Proc. IEEE Comput. Soc. Conf. Comput. Vis. Pattern Recognit. 2016-Decem (2016) 770–778. https://doi.org/10.1109/CVPR.2016.90.

[70] G. Huang, Z. Liu, L. van der Maaten, K.Q. Weinberger, Densely Connected Convolutional Networks, in: Comput. Vis. Pattern Recognit. Conf., 2017. https://doi.org/https://doi.org/10.48550/arXiv.1608.06993.

[71] A. Howard, M. Sandler, B. Chen, W. Wang, L.-C. Chen, M. Tan, G. Chu, V. Vasudevan, Y. Zhu, R. Pang, H. Adam, Q. Le, Searching for MobileNetV3, in: 2019 IEEE/CVF Int. Conf. Comput. Vis., IEEE, 2019: pp. 1314–1324. https://doi.org/10.1109/ICCV.2019.00140.

[72] J. Xu, R.D. Deshpande, J. Pan, Y.-T. Cheng, V.S. Battaglia, Electrode Side Reactions, Capacity Loss and Mechanical Degradation in Lithium-Ion Batteries, J. Electrochem. Soc. 162 (2015) A2026–A2035. https://doi.org/10.1149/2.0291510jes.

[73] https://evwest.com/support/panasonic-ncr18650bd-datasheet.pdf, Panasonic NCR 18650BD Datasheet, (n.d.).

[74] R. Spotnitz, J. Franklin, Abuse behavior of high-power, lithium-ion cells, J. Power Sources. 113 (2003) 81–100. https://doi.org/10.1016/S0378-7753(02)00488-3.

[75] G.H. Kim, A. Pesaran, R. Spotnitz, A three-dimensional thermal abuse model for lithium-ion cells, J. Power Sources. 170 (2007) 476–489. https://doi.org/10.1016/j.jpowsour.2007.04.018.

[76] X. Feng, S. Zheng, D. Ren, X. He, L. Wang, H. Cui, X. Liu, C. Jin, F. Zhang, C. Xu, H. Hsu, S. Gao, T. Chen, Y. Li, T. Wang, H. Wang, M. Li, M. Ouyang, Investigating the

thermal runaway mechanisms of lithium-ion batteries based on thermal analysis database, Appl. Energy. 246 (2019) 53–64. https://doi.org/10.1016/j.apenergy.2019.04.009.

[77] V. Jabbari, V. Yurkiv, M.G. Rasul, M.T. Saray, R. Rojaee, F. Mashayek, R. Shahbazian-Yassar, An efficient gel polymer electrolyte for dendrite-free and long cycle life lithium metal batteries, Energy Storage Mater. 46 (2022) 352–365. https://doi.org/10.1016/j.ensm.2022.01.031.

[78] P. Ramadass, B. Haran, R. White, B.N. Popov, Mathematical modeling of the capacity fade of Li-ion cells, J. Power Sources. 123 (2003) 230–240. https://doi.org/10.1016/S0378-7753(03)00531-7.

[79] X. Lin, J. Park, L. Liu, Y. Lee, A.M. Sastry, W. Lu, A Comprehensive Capacity Fade Model and Analysis for Li-Ion Batteries, J. Electrochem. Soc. 160 (2013) A1701–A1710. https://doi.org/10.1149/2.040310jes.

[80] C. Zu, H. Yu, H. Li, Enabling the thermal stability of solid electrolyte interphase in Li-ion battery, InfoMat. 3 (2021) 648–661. https://doi.org/10.1002/inf2.12190.

[81] I. Kandel, M. Castelli, The effect of batch size on the generalizability of the convolutional neural networks on a histopathology dataset, ICT Express. 6 (2020) 312–315. https://doi.org/10.1016/j.icte.2020.04.010.

[82] N. Buduma, N. Locascio, Fundamentals of Deep Learning: Designing Next-Generation Machine Intelligence Algorithms, 1st ed., O'Reilly Media, Inc., 2017. https://dl.acm.org/doi/10.5555/3161223.

[83] T. Saranya, C. Deisy, S. Sridevi, K.S. Muthu, M.K.A.A. Khan, Performance Analysis of First Order Optimizers for Plant Pest Detection Using Deep Learning, in: 2022: pp. 37–52. https://doi.org/10.1007/978-3-031-24367-7_4.

[84] D.M.W. Powers, Evaluation: from precision, recall and F-measure to ROC, informedness, markedness and correlation, Int. J. Mach. Learn. Technol. (2020) 37–63. http://arxiv.org/abs/2010.16061.

[85] C.P. Papageorgiou, M. Oren, T. Poggio, A general framework for object detection, in: Sixth Int. Conf. Comput. Vis. (IEEE Cat. No.98CH36271), Narosa Publishing House, n.d.: pp. 555–562. https://doi.org/10.1109/ICCV.1998.710772.

[86] Y. Yu, X. Si, C. Hu, J. Zhang, A Review of Recurrent Neural Networks: LSTM Cells and Network Architectures, Neural Comput. 31 (2019) 1235–1270. https://doi.org/10.1162/neco_a_01199.

[87] S. Zhang, H. Tong, J. Xu, R. Maciejewski, Graph convolutional networks: a comprehensive review, Comput. Soc. Networks. 6 (2019) 11. https://doi.org/10.1186/s40649-019-0069-y.

[88] B.R. Das Goswami, M. Mastrogiorgio, M. Ragone, V. Jabbari, R. Shahbazian-Yassar, F. Mashayek, V. Yurkiv, A combined multiphysics modeling and deep learning framework to predict thermal runaway in cylindrical Li-ion batteries, J. Power Sources. 595 (2024) 234065. https://doi.org/10.1016/j.jpowsour.2024.234065.

[89] https://industrial.panasonic.com/ww/products/pt/lithium-ion/models, Panasonic Lithium Ion Battery Models, (n.d.).

[90] M. Steinhardt, E.I. Gillich, A. Rheinfeld, L. Kraft, M. Spielbauer, O. Bohlen, A. Jossen, Low-effort determination of heat capacity and thermal conductivity for cylindrical 18650 and 21700 lithium-ion cells, J. Energy Storage. 42 (2021) 103065. https://doi.org/10.1016/j.est.2021.103065.

[91] S.P.V. Nadimpalli, V.A. Sethuraman, D.P. Abraham, A.F. Bower, P.R. Guduru, Stress

Evolution in Lithium-Ion Composite Electrodes during Electrochemical Cycling and Resulting Internal Pressures on the Cell Casing, J. Electrochem. Soc. 162 (2015) A2656–A2663. https://doi.org/10.1149/2.0341514jes.

[92] E. Hosseinzadeh, R. Genieser, D. Worwood, A. Barai, J. Marco, P. Jennings, A systematic approach for electrochemical-thermal modelling of a large format lithium-ion battery for electric vehicle application, J. Power Sources. 382 (2018) 77–94. https://doi.org/10.1016/j.jpowsour.2018.02.027.

[93] R. Fu, S.-Y. Choe, V. Agubra, J. Fergus, Development of a physics-based degradation model for lithium ion polymer batteries considering side reactions, J. Power Sources. 278 (2015) 506–521. https://doi.org/10.1016/j.jpowsour.2014.12.059.

[94] S.P.V. Nadimpalli, V.A. Sethuraman, D.P. Abraham, A.F. Bower, P.R. Guduru, Stress Evolution in Lithium-Ion Composite Electrodes during Electrochemical Cycling and Resulting Internal Pressures on the Cell Casing, J. Electrochem. Soc. 162 (2015) A2656–A2663. https://doi.org/10.1149/2.0341514jes.

[95] E. Hosseinzadeh, R. Genieser, D. Worwood, A. Barai, J. Marco, P. Jennings, A systematic approach for electrochemical-thermal modelling of a large format lithium-ion battery for electric vehicle application, J. Power Sources. 382 (2018) 77–94. https://doi.org/10.1016/j.jpowsour.2018.02.027.

[96] R. Fu, S.-Y. Choe, V. Agubra, J. Fergus, Development of a physics-based degradation model for lithium ion polymer batteries considering side reactions, J. Power Sources. 278 (2015) 506–521. https://doi.org/10.1016/j.jpowsour.2014.12.059.

[97] F.E. Szabo, A, in: Linear Algebr. Surviv. Guid., Elsevier, 2015: pp. 11–38. https://doi.org/10.1016/B978-0-12-409520-5.50008-4.

[98] B. Yu, H. Yin, Z. Zhu, Spatio-Temporal Graph Convolutional Networks: A Deep Learning Framework for Traffic Forecasting, in: Proc. Twenty-Seventh Int. Jt. Conf. Artif. Intell. {IJCAI-18}, International Joint Conferences on Artificial Intelligence Organization, 2018: pp. 3634–3640. https://doi.org/10.24963/ijcai.2018/505.

[99] J. Zhou, G. Cui, S. Hu, Z. Zhang, C. Yang, Z. Liu, L. Wang, C. Li, M. Sun, Graph neural networks: A review of methods and applications, AI Open. 1 (2020) 57–81. https://doi.org/10.1016/j.aiopen.2021.01.001.

[100] A. Sherstinsky, Fundamentals of Recurrent Neural Network (RNN) and Long Short-Term Memory (LSTM) network, Phys. D Nonlinear Phenom. 404 (2020) 132306. https://doi.org/10.1016/j.physd.2019.132306.

[101] T. Waldmann, R.-G. Scurtu, K. Richter, M. Wohlfahrt-Mehrens, 18650 vs. 21700 Li-ion cells – A direct comparison of electrochemical, thermal, and geometrical properties, J. Power Sources. 472 (2020) 228614. https://doi.org/10.1016/j.jpowsour.2020.228614.

[102] J. Belt, A. Sorensen, Thermal and Electrochemical Analysis of Thermal Runaway Propagation of Samsung Cylindrical Cells in Lithium-ion Battery Modules, J. Electrochem. Soc. 170 (2023) 010515. https://doi.org/10.1149/1945-7111/aca939.

[103] Y. Jia, J. Li, W. Yao, Y. Li, J. Xu, Precise and fast safety risk classification of lithium-ion batteries based on machine learning methodology, J. Power Sources. 548 (2022) 232064. https://doi.org/10.1016/j.jpowsour.2022.232064.